Cellulose Synthase Complex and Remorin Nanodomains Mediate Stress Resilience Through Cell Wall-Plasma Membrane Attachments

Authors: Yue Rui[1,*], Andres V. Reyes[2,3], Tarabryn S. Grismer[2,3], Nikolaj B. Abel[4], William P. Dwyer[1], Thomas Ott[5,6], Joseph J. Kieber[7], Shou-Ling Xu[2,3], and José R. Dinneny[1,8,*]

Affiliations:
[1]Department of Biology, Stanford University, Stanford, CA 94305, USA
[2]Division of Biosphere Science and Engineering, Carnegie Institution for Science, Stanford, CA 94305, USA
[3]Carnegie Mass Spectrometry Facility, Carnegie Institution for Science, Stanford, CA 94305, USA
[4]Department of Molecular Biology and Genetics, Aarhus University, Aarhus, 8000, Denmark
[5]Faculty of Biology, University of Freiburg, 79104 Freiburg, Germany
[6]CIBSS - Centre for Integrative Biological Signalling Studies, University of Freiburg, 79104 Freiburg, Germany
[7]Department of Biology, University of North Carolina, Chapel Hill, NC 27599, USA
[8]Howard Hughes Medical Institute, Stanford University, Stanford, CA 94305, USA
*Correspondence: yuerui@stanford.edu (Y.R.), dinneny@stanford.edu (J.R.D.)

Highlights

- The plasma membrane forms attachments to the plant cell wall that are revealed by hyperosmotic shock and correlate to the tolerance of root growth to stress.
- Cellulose Synthase Complex (CSC) and REMORIN (REM) nanodomains localize to cell wall-plasma membrane attachment sites.
- CSC density at the plasma membrane determines the extent of cell wall-plasma membrane attachment under hyperosmotic stress.
- REM nanodomains form rapidly under hyperosmotic stress and harbor the CSC exocytosis inhibitors SHOU4/4L, which limit CSC density at the plasma membrane.

Summary

The outer cell surface of an organism is the frontline for detecting and responding to environmental stimuli. In plants, this interface consists of the plasma membrane that lies beneath the cell wall and remains associated with it through attachment sites. These wall-membrane attachments become evident upon hyperosmotic shock, when severe water loss causes the membrane to retract from the wall. Despite their long-standing observation, the molecular identity and function of these attachments remain poorly understood. Here, we identified two nanodomain-mediated mechanisms governing wall-membrane attachments: one dependent on the Cellulose Synthase Complex (CSC), whose density at the plasma membrane positively correlates with resistance to hyperosmotic stress, and the other on REMORIN (REM), which acts antagonistically to the CSC mechanism. Using proximity-labeling proteomics, we identified SHOU4/4L as REM-associated proteins that mediate this antagonism. Together, our

findings reveal how membrane nanodomains pattern wall-membrane attachments to mediate plant cell resilience under water stress.

Introduction

Living organisms must sense and respond to changing environments for their survival. The outer cell surface represents the frontline in this process and comprises an extracellular matrix that surrounds the cell and interfaces with the plasma membrane, where signaling is integrated and communicated to the cell through receptors and other membrane-associated proteins. A fundamental understanding of the organization, dynamics, and composition of this outer cell surface will shed light on the molecular underpinnings of stress perception and acclimation. In animal cells, the plasma membrane is anchored to the extracellular matrix by integrins,[1] transmembrane receptors that serve as structural and signaling hubs for sensing and transmitting mechanochemical cues at the cell surface.[2] Integrins have not been found in plants,[3,4] however, and it remains unclear what molecules in the cell wall and the plasma membrane mediate their attachment, how the cell wall-plasma membrane interface is maintained and remodeled during environmental stress, and how signals are perceived at this interface in response to changes in internal (e.g., turgor pressure) or external cues (e.g., chemical or mechanical stimuli).

The plant cell wall is a polysaccharide-based extracellular matrix comprised of cellulose microfibrils embedded in a molecular network composed of hemicelluloses, pectins, and structural proteins.[5] Plant cell walls play key roles in defining cell shape, providing structural support, and mediating cellular signaling.[6,7] The cell wall constrains the lateral diffusion of plasma membrane proteins[8] and regulates the size and dynamics of membrane nanodomains,[9] which are submicron molecular assemblies with diverse protein and lipid compositions.[10,11] Much of our understanding of cell wall function has come from studies in *Arabidopsis thaliana*, particularly through the characterization of mutants impaired in the synthesis, modification, or degradation of specific wall components.[5] A number of studies have demonstrated the effects that environmental stress has on cell wall properties, and the physiological impact that disruptions in cell wall composition have on the ability of plants to acclimate to such stresses.[7,12] However, whether specific wall constituents play a role in mediating wall-membrane attachments has not been determined.

Under non-stress conditions, turgor pressure appresses the plasma membrane against the cell wall (Figure 1). However, under hyperosmotic stress, cellular water loss can be so severe that plasmolysis ensues, when the plasma membrane retracts from the cell wall (Figure 1C-1E, Video S1). Notably, during plasmolysis, portions of the plasma membrane remain attached to the cell wall, forming thin connecting membrane filaments known as Hechtian strands, first described by Hecht over a century ago.[13] These strands are part of a larger network collectively referred to as the Hechtian structure,[14] which includes Hechtian strands, the Hechtian reticulum, and wall-membrane attachment sites. The attachment sites, located at the distal ends of Hechtian structures (Figure 1D and 1E, Video S1) are reminiscent of focal adhesions in mammalian cells,[15] yet their molecular identity and function remain largely unknown.[3,4] Some

Hechtian structures are likely attached to the wall via plasmodesmata,[14] membrane-lined intercellular channels that mediate transport and communication between plant cells. However, the presence of wall-membrane attachment sites at the outer surface of epidermal cells[3] and in guard cells,[16] both of which lack plasmodesmata, suggests alternative mechanisms for connecting the cell wall and the plasma membrane.

The plasma membrane is a lipid bilayer enriched with diverse lipid species and proteins, and it exhibits heterogeneity in its physicochemical properties.[17] Importantly, many membrane proteins are organized into nanodomains to fulfill their functions in plant growth, abiotic stress responses, and biotic interactions.[10,11] For example, Cellulose Synthase Complexes (CSCs) form discrete puncta at the plasma membrane[18] and are considered nanodomains by microscopy-based definitions.[10] CSCs have been proposed to anchor the plasma membrane to the cell wall in plasmolyzed plant cells through the nascently synthesized cellulose microfibrils that become embedded into the wall matrix,[19] yet this idea remains experimentally untested. Hyperosmotic stress can also induce the formation of nanodomains, which was recently demonstrated for ROP6, a Rho GTPase that interacts with NADP oxidases to produce reactive oxygen species important for osmotic signaling.[20] In the context of biotic interactions, REMORINs (REMs) are a well-characterized protein family known to organize into nanodomains.[21] For instance, the symbiosis-specific remorin SYMREM1 in *Medicago truncatula* is essential for stabilizing the symbiotic receptor-like kinase LYK3[22] and maintaining membrane topology during infection.[23] Interestingly, *in vitro* studies have shown that REMs can bind oligo- and polygalacturonides,[24] components of pectins in the cell wall. However, whether REMs contribute to physical or functional associations between the cell wall and plasma membrane is unknown.

Plant roots absorb water and nutrients from the environment, and their growth is highly sensitive to environmental fluctuations. Here, we leveraged the effects of hyperosmotic stress to investigate the structure and function of the cell wall-plasma membrane interface in roots. We demonstrate that maintaining CSC density at the plasma membrane is essential for wall-membrane attachments and sustained root growth under hyperosmotic stress conditions. We show that wall-membrane attachment sites contain two populations of nanodomains, CSCs and REMs, respectively. Genetic, biochemical, and co-localization studies identified SHOU4/4L, known negative regulators of CSC exocytosis,[25] as being associated with REM nanodomains that limit CSC density at the plasma membrane. Our data support a one-way antagonistic mechanism where REM nanodomains restrict the abundance of CSC nanodomains. CSCs and REMs function together at the plasma membrane to regulate wall-membrane attachments, which are critical for maintaining cellular resilience under water deficit conditions.

Results

Impaired cellulose and rhamnose levels have contrasting effects on root growth under hyperosmotic stress

To investigate the roles of cell wall polysaccharides in hyperosmotic stress response, we surveyed a collection of previously published Arabidopsis mutants deficient in cellulose,

133 xyloglucan (a hemicellulose), pectic homogalacturonan (HG), rhamnogalacturonan-I (RG-I), or
134 rhamnogalacturonan-II (RG-II), respectively, for changes in root growth (Figure S1A, Figure 2).
135 Under hyperosmotic stress induced by 0.28 M sorbitol, wild-type roots exhibited a growth
136 reduction of 52-57% compared to the control conditions (Figure 2, Figure S1B). Mutants lacking
137 cellulose, including *cesa3*^{je5}, *cesa6*$^{prc1-1}$, and *cob-1*, all displayed a more severe growth
138 reduction (≥75%) (Figure 2A). Expression of *GFP-CESA3* under its native promoter in the
139 *cesa3*^{je5} mutant background restored root growth to wild-type levels (Figure 2A).
140
141 Mutants defective in xyloglucan (Figure 2B), HG (Figure 2C), RG-I acetylation (Figure 2D), or
142 RG-II crosslinking (Figure 2E) generally showed wild-type responses to stress. The only
143 exception was *qua2-1*, which exhibited a significantly greater reduction in root growth compared
144 to wild type under stress (Figure 2C), though this may be influenced by its known defects in cell-
145 cell adhesion.[26]
146
147 In contrast to the cellulose mutants, the *rhm1-1*, *rhm1-2*, and *rhm1-3* mutants, which are
148 deficient in rhamnose, a component of the RG-I backbone,[27] showed significantly less reduction
149 in root growth under hyperosmotic stress than the wild type (Figure 2D and Figure S1B). This
150 phenotype was reversed by expressing *RHM1-GFP* under its native promoter (Figure 2D).
151 Rhamnose in RG-I can be substituted with side chains, including *α*-1,5-arabinan and *β*-1,4-
152 galactan. While a deficiency in galactan, as in the *gals1/2/3* mutants,[28] partially mirrored the
153 *rhm1* mutant's response, a deficiency in arabinan, as in the *mur4-1* mutant, did not show a
154 similar effect (Figure 2D). Taken together, our mutant survey suggests specific but contrasting
155 roles of cellulose and RG-I rhamnose in root growth responses to hyperosmotic stress.
156
157 *Deficiency in cellulose or rhamnose has opposite effects on plasmolysis and baseline plasma*
158 *membrane proteome*
159
160 To further understand the functions of cellulose and rhamnose in hyperosmotic stress response
161 at the cellular and molecular level, we performed live-cell imaging of five-day-old seedlings
162 expressing YFP-LTI6b, a classic plasma-membrane marker, after a brief hyperosmotic stress
163 treatment. The 0.28 M sorbitol concentration used in our root growth assay (Figure 2) did not
164 cause any noticeable changes in root cells compared to the control condition (Figure S1C).
165 However, treatment with 0.5 M sorbitol induced plasmolysis, with the plasma membrane
166 detaching from the cell wall at cell-cell junctions along the root's longitudinal axis (Figure S1C).
167 Increasing the sorbitol concentration to 1 M caused a more pronounced plasmolysis effect, with
168 the membrane also retracting from the outer periphery of root cells. Hechtian structures and cell
169 wall-plasma membrane attachment sites were clearly visible at these membrane retraction sites
170 (Figure S1C, Figure 1C-1E).
171
172 We selected 0.5 M sorbitol to compare plasmolysis in the wild type, cellulose-deficient, and
173 rhamnose-deficient mutants, as this concentration is less stressful than 1 M sorbitol and allows
174 for easier quantification of plasmolysis by area. The ratio of protoplast area (highlighted by YFP-
175 LTI6b) to cell area (outlined by the cell wall in the bright field channel) was used as a measure

176 of plasmolysis. Compared to wild-type cells, plasmolysis was more severe in the *cesa3*^{je5}
177 mutant, with a greater proportion of cells displaying lower ratios between 0.6-0.8 (26% in
178 *cesa3*^{je5} vs. 12% in wild type) (Figure 3A and 3B). In contrast, 70% of the *rhm1-1* cells exhibited
179 minimal plasmolysis at a ratio between 0.9-1.0, whereas this proportion in the wild type is 34%
180 (Figure 3A and 3B). These cellular-level plasmolysis results correlate with the severity with
181 which root growth was inhibited in these mutants (Figure 2A and 2D).
182
183 To identify membrane protein signatures underlying the distinctive hyperosmotic stress
184 responses of *cesa3*^{je5} and *rhm1-1* mutants, we used a biotin ligase-based proximity labeling
185 approach[29,30] by expressing a TurboID (TbID)-YFP-LTI6b fusion protein in the respective
186 genetic backgrounds. After confirming that TbID-YFP-LTI6b localized to the plasma membrane
187 (Figure S2A), we treated five-day-old seedlings with 50 μM biotin for 15 min (Figure 3C), which
188 was sufficient to biotinylate proteins beyond the endogenously biotinylated ones, as confirmed
189 by western blotting (Figure S2B and S2C). Following protein extraction, streptavidin pull-down of
190 the biotinylated proteins, tryptic digestion, and mass spectrometry, we conducted pairwise
191 protein enrichment analyses between each mutant and the wild type (Figure S2D and S2E).
192
193 In the *cesa3*^{je5} mutant, only one protein exhibited differential labeling: TOM1-LIKE1 (TOL1),[31,32]
194 which was significantly less enriched compared to wild type (Figure 3D). In contrast, over a
195 thousand proteins showed differential enrichment in the *rhm1-1* mutant relative to wild type
196 (Figure 3E). Among the most enriched proteins were CESA1, CESA5, CESA6, CELLULOSE
197 SYNTHASE-INTERACTIVE1 (CSI1),[33,34] CSI3,[35] PATROL1,[36] and CMU1[37] (Figure 3E), which
198 are involved in cellulose synthesis, CSC delivery to the plasma membrane, or microtubule
199 stability to guide CSC movement. These differences in enrichment were not caused by changes
200 in LTI6b levels, which were consistent across all transgenic lines. These data suggest that
201 defects in RG-I rhamnose biosynthesis lead to an increase in the abundance of CSC-associated
202 proteins at the plasma membrane.
203
204 To directly measure CSC density at the plasma membrane in root cells and assess its changes
205 due to deficiencies in cellulose or rhamnose, we introduced the GFP-CESA3 marker, driven by
206 its native promoter, into the wild-type, *cesa6*$^{prc1-1}$, and *rhm1-1* backgrounds. Similar to earlier
207 reports in etiolated hypocotyls,[18] CSCs were observed at the plasma membrane as particles
208 near or below the resolution limit of the spinning disk confocal microscope, and in Golgi as
209 bright "disks" larger than the membrane-localized particles (Figure 3F). Compared to the wild
210 type, GFP-CESA3-labeled CSC particles in *cesa6*$^{prc1-1}$ roots were barely detectable at the
211 plasma membrane, though Golgi-localized CSCs remained visible (Figure 3F and 3G). In
212 contrast, *rhm1-1* roots exhibited a significantly higher CSC particle density at the plasma
213 membrane than wild-type roots (Figure 3F and 3G), consistent with our proteomic
214 characterization (Figure 3E).
215
216 *CSCs mediate cell wall-plasma membrane attachments under hyperosmotic stress*
217
218 Our results thus far point to a possible link between CSC density at the plasma membrane and
219 the severity of plasmolysis during hyperosmotic stress, suggesting that CSC may be directly or

220 indirectly involved in promoting wall-membrane attachments. To test this hypothesis, we
221 crossed the tdTomato-CESA6 marker with GFP-LTI6b and imaged root cells using spinning disk
222 confocal microscopy. Under control conditions, tdTomato-CESA6-labeled CSCs appeared as
223 particles that move along linear trajectories at the plasma membrane (Figure 4A, Figure S3A,
224 Video S2), consistent with previous observations in etiolated hypocotyls.[18] Treatment with 1 M
225 sorbitol immobilized CSCs into nanodomains at the plasma membrane (Figure S3A, Video S3),
226 which showed an increased degree of signal overlap with GFP-LTI6b-labeled wall-membrane
227 attachment sites compared to the control condition (Figure 4A and 4B, Video S4). Because
228 cortical microtubules guide the distribution of CSCs at the plasma membrane,[18,38] we also
229 examined how incipient hyperosmotic stress affects microtubules and their colocalization with
230 CSCs using the GFP-CESA3/mCherry-TUA5 double marker line.[38] In Hechtian structures where
231 the plasma membrane remained attached to the cell wall, mCherry-TUA5-labeled microtubules
232 appeared as strand-like structures, which were decorated by the immobilized population of
233 CSCs at the plasma membrane (Figure S3B).
234
235 To determine whether the plasma membrane-localized CSCs mediate wall-membrane
236 attachments, we treated YFP-LTI6b seedlings with the cellulose biosynthesis inhibitor isoxaben
237 (ISX), which has previously been shown to remove CSCs from the plasma membrane.[18] After
238 confirmation of this CSC clearance (Figure S3C and S3D), we induced plasmolysis with 0.5 M
239 sorbitol and quantified the degree of plasmolysis (Figure 4C). Compared to the mock condition,
240 ISX treatment resulted in a greater fraction of cells exhibiting increased plasmolysis (Figure 4D).
241 This trend is consistent with that observed in the cellulose-deficient mutants *cesa3*^{je5} (Figure 3A
242 and 3B) and *cesa6*$^{prc1-1}$ (Figure 4E). Additionally, ISX caused changes in protoplast morphology
243 under 0.5 M sorbitol, specifically enhancing curvature at both ends (Figure 4C, Figure S3E). To
244 further assess the impact of ISX on wall-membrane attachments at the outer cell surface, we
245 induced plasmolysis using 1 M sorbitol. In mock-treated roots, wall-membrane attachment sites
246 were evident in regions where the plasma membrane had dissociated from the wall of the outer
247 cell surface. In contrast, in ISX-treated roots, protoplast detachment and shrinkage occurred
248 primarily at the cell-cell junctions (Figure 4F). These data confirm that wall-membrane
249 attachment sites contain CSCs, which are necessary for the physical stability of these
250 associations during hyperosmotic stress.
251
252 To further test this hypothesis, we analyzed another cell wall mutant, *shou4-3 4l-1*, which lacks
253 the negative regulators of CSC exocytosis, SHOU4 and SHOU4L, and was previously shown to
254 exhibit a higher CSC density at the plasma membrane relative to the wild type.[25] Root growth
255 reduction under hyperosmotic stress was significantly less severe in *shou4-3 4l-1* compared to
256 the wild type (Figure 4G). Moreover, the proportion of root cells in this mutant that exhibit no
257 measurable wall-membrane detachment was substantially higher than that in the wild type
258 (Figure 4H), resembling the phenotypes observed in the *rhm1-1* mutants (Figure 2D, Figure 3A
259 and 3B). The *cesa6*$^{prc1-1}$ *shou4-1* double mutant,[25] however, displayed root growth phenotypes
260 similar to the *cesa6*$^{prc1-1}$ single mutant (Figure S3F, Figure 2A), suggesting that the *cesa6*$^{prc1-1}$
261 mutation is epistatic to the *shou4-1* mutation. Similarly, the *cesa3*^{je5} mutation was epistatic to
262 *rhm1-1* in root growth under both control and hyperosmotic stress conditions (Figure 4I, Figure
263 2A). As a complementary approach, we tested the effect of ISX on root growth in the *rhm1-1*

264 mutant or *shou4-3 4l-1* double mutant and found that this treatment similarly led to a more
265 severe degree of growth reduction than the non-ISX treated controls (Figure 4J). These results
266 indicate that CSCs act downstream of *RHM1* and *SHOU4/4L*.
267
268 Together, these data suggest that CSC density at the plasma membrane safeguards
269 hyperosmotic stress responses in roots by mediating wall-membrane attachments.
270
271 *REMs rapidly form nanodomains at wall-membrane attachment sites upon hyperosmotic stress*
272
273 CSCs are organized, by definition,[10] in nanodomains under both control and hyperosmotic
274 stress conditions (Figure 4A). To investigate how other plasma membrane nanodomains
275 respond to hyperosmotic stress, we focused on REMs, the best-characterized markers of
276 plasma membrane nanodomains[39] and known stabilizers of membrane topologies.[23] Using live-
277 cell laser scanning confocal microscopy in five-day-old seedling roots expressing YFP-REM1.2,
278 we observed a diffuse yet polarized localization, with stronger fluorescence signals detected at
279 the shootward regions of the plasma membrane (Figure 5A). Upon treatment with sorbitol for 5
280 minutes, YFP-REM1.2 coalesced into nanodomains that are approximately 0.4 μm in diameter,
281 and their density increased in a concentration-dependent manner with sorbitol (Figure 5A and
282 5B). This suggests that the density of YFP-REM1.2-positive nanodomains serves as a readout
283 for the severity of hyperosmotic stress. Similar nanodomain formation was observed in other
284 tissues, including cotyledons and hypocotyls, when treated with sorbitol (Figure S4A). Because
285 REMs are also components of plasmodesmata-localized nanodomains,[40] we crossed a
286 plasmodesmata marker, mCherry-PDCB1,[41] with YFP-REM1.2 to study their co-association. At
287 cell-cell junctions, a portion of YFP-REM1.2 nanodomains overlapped with mCherry-PDCB1
288 signal (Figure S4B), confirming their presence in plasmodesmata. However, YFP-REM1.2
289 nanodomains observed on the outer (periclinal) sides of cells were independent of
290 plasmodesmata (Figure S4B). Our study focused on this latter population of YFP-REM1.2
291 nanodomains. Time-lapse imaging revealed rapid formation of these immobile nanodomains,
292 likely instantaneously upon hyperosmotic stress (Figure S4C, Video S5). Notably, this process
293 was reversible: the nanodomains dispersed back into the plasma membrane when
294 hyperosmotic stress was alleviated (Video S6). Lastly, to evaluate the dependence of YFP-
295 REM1.2 nanodomain formation on sterols, a key membrane lipid species that facilitates REM
296 localization into highly ordered nanodomains[39], we treated YFP-REM1.2 seedlings with
297 fenpropimorph, a sterol biosynthesis inhibitor.[42] Unlike the mock-treated control, fenpropimorph-
298 treated seedlings did not exhibit YFP-REM1.2 nanodomains under hyperosmotic stress (Figure
299 S4D). These results suggest that the formation of YFP-REM1.2 nanodomains relies on the
300 sterol composition of the plasma membrane.
301
302 To test whether YFP-REM1.2 nanodomains are associated with wall-membrane attachment
303 sites, we performed live-cell imaging experiments using two approaches: staining five-day-old
304 YFP-REM1.2 seedlings with calcofluor white (Figure 5C) and generating a YFP-
305 REM1.2/mCherry-LTI6b double marker line (Figure 5D). Hyperosmotic stress-induced YFP-
306 REM1.2 nanodomains were attached to the wall (Figure 5C) and remained colocalized with
307 mCherry-LTI6b-labeled wall-membrane attachment sites at the outer surface of cells (Figure 5D

308 and 5E). To investigate the role of REMs in hyperosmotic stress responses, we analyzed the
309 *rem1.2 1.3* double mutant[40,43] and the *rem1.2 1.3 1.4* triple mutant[43] by assessing root growth
310 and plasmolysis. *rem1.2 1.3* double mutants did not differ from the wild type (Figure S4E and
311 S4F), while *rem1.2 1.3 1.4* triple mutants displayed significantly reduced growth inhibition and
312 resistance to plasmolysis under stress conditions (Figure 5F-5H), phenotypes that were similar
313 to those of the *rhm1* and *shou4-3 4l-1* mutants (Figure 2D, Figure 3A and 3B, Figure 4G and
314 4H). Expression of YFP-REM1.2 under its native promoter in the *rem1.2 1.3 1.4* triple mutant
315 background restored the root growth phenotypes to wild-type levels (Figure 5F). Together, these
316 results suggest that the rapidly forming REM nanodomains function as negative regulators of
317 wall-membrane attachments.
318
319 *REMs antagonize CSCs to regulate hyperosmotic stress responses*
320
321 Given the observed formation of CSC nanodomains and REM nanodomains in root cells under
322 hyperosmotic stress, we next sought to investigate the relationship between these two
323 nanodomain populations. To visualize them, we crossed YFP-REM1.2 with tdTomato-CESA6
324 lines and imaged root cells using spinning disk confocal microscopy under control conditions or
325 in the presence of 1 M sorbitol. Under control conditions, tdTomato-CESA6-labeled CSC
326 particles were distributed across the plasma membrane, while YFP-REM1.2 signals were
327 predominantly localized to the shootward regions of the plasma membrane (Figure 6A). Upon
328 treatment with 1 M sorbitol, both markers formed distinct nanodomains (Figure 6A and 6B). To
329 quantify the spatial relationship of CSCs and REMs, we performed Manders' colocalization
330 analysis using the GFP-CESA3/tdTomato-CESA6 double marker line as a positive control
331 (Figure S5A). Under control conditions, YFP-REM1.2 signals showed minimal overlap with
332 tdTomato-CESA6-labeled CSC particles (Figure 6C). However, under hyperosmotic stress,
333 REM1.2 and CSC nanodomains exhibited partial colocalization, yet their Manders' overlap
334 coefficients remained significantly lower than those of the GFP-CESA3/tdTomato-CESA6
335 positive control (Figure 6C). These data suggest that CSCs and REMs function in spatially
336 distinct cellular domains under hyperosmotic stress, though partial colocalization suggests there
337 may be specific cellular contexts where their function may be coordinated.
338
339 To determine whether there is a functional relationship between the distribution of these two
340 nanodomains, we introduced the YFP-REM1.2 marker into the *cesa3*^{je5} and *rhm1-1* mutant
341 backgrounds and measured REM nanodomain density following 0.5 M sorbitol treatment. While
342 REM nanodomain density in the *cesa3*^{je5} mutant remained unchanged, it was significantly
343 reduced in the *rhm1-1* mutant compared to the wild type (Figure 6D and 6E), suggesting that
344 RHM1 promotes REM nanodomain formation. Additionally, we introduced the GFP-CESA3
345 marker into the *rem1.2 1.3 1.4* triple mutant and quantified CSC density at the plasma
346 membrane under control conditions. *rem1.2 1.3 1.4* triple mutants exhibited significantly higher
347 CSC density than wild type (Figure 6F and 6G). Given the importance of sterol biosynthesis for
348 REM1.2 nanodomain formation (Figure S4D), we tested whether it also influences CSC
349 patterning at the plasma membrane and affects plasmolysis. Compared to mock-treated roots,
350 treatment with fenpropimorph had no detectable effect on CSC density at the plasma membrane
351 or on protoplast behavior under 0.5 M sorbitol (Figure S5B-S5E). These data support the

352 hypothesis that CSC density at the plasma membrane is necessary for plasma membrane-cell
353 wall attachment, which plays a critical role in safeguarding root cells against the disruptive effect
354 of hyperosmotic stress. Furthermore, our data suggest that REMs inhibit the formation of these
355 attachments by limiting CSCs abundance at the plasma membrane, independently of REM
356 nanodomain formation.
357
358 To test this hypothesis, we analyzed the effect of ISX on hyperosmotic stress-induced growth
359 inhibition in *rem1.2 1.3 1.4* triple mutant roots. Under sorbitol treatment, mock-treated mutants
360 exhibited a 52% reduction in growth, whereas ISX treatment exacerbated the reduction to 83%
361 (Figure 6H), a level comparable to that observed in cellulose-deficient mutants (Figure 2A). We
362 also generated the *cesa3*^{je5} *rem1.2 1.3* triple mutant and found that this line phenocopied the
363 *cesa3*^{je5} single mutant under both control and hyperosmotic stress conditions (Figure 6I, Figure
364 2A). We further attempted to generate the *cesa3*^{je5} *rem1.2 1.3 1.4* quadruple mutant but were
365 unsuccessful because the *cesa3*^{je5} and *rem1.4* mutations are located on the same arm of
366 chromosome 5. Together, these results confirm that the reduced severity of hyperosmotic stress
367 responses in *rem1.2 1.3 1.4* triple mutants is a consequence of enhanced CSC density at the
368 plasma membrane, and further suggest an antagonistic relationship between REMs and CSCs.
369
370 *SHOU4/4L are components of REM nanodomains*
371
372 To uncover additional proteins present in REM nanodomains that could mediate the apparent
373 antagonism with CSCs, we employed proximity labeling and generated transgenic lines
374 expressing *TbID-YFP-REM1.2* driven by the *REM1.2* native promoter in the wild-type
375 background. After confirming that the TbID tag did not affect YFP-REM1.2 localization to the
376 plasma membrane or nanodomain formation (Figure S6A), we treated five-day-old seedlings
377 with 50 μM biotin for 15 minutes, in the presence or absence of 0.5 M sorbitol. In both
378 conditions, biotinylated proteins were detected in addition to those that are endogenously
379 biotinylated (Figure S6B and S6C). Overall, we identified 5,922 proteins, which were subjected
380 to two filtering steps (Figure 7A). To eliminate background proteins, we compared TbID-YFP-
381 REM1.2 samples with the wild-type control, identifying 30 and 111 proteins under the control
382 and sorbitol-treated conditions, respectively (Figure 7B and 7C). A subsequent comparison
383 between these conditions revealed 83 proteins enriched specifically under sorbitol treatment
384 (Figure 7D).
385
386 Our proteomic data revealed proteins known to interact with REM1.2, including REM1.2 itself,
387 REM1.3 and other REMs in the same family,[43] RPM1-INTERACTING PROTEIN4 (RIN4),[44] and
388 PLASMA-MEMBRANE ASSOCIATED CATION-BINDING PROTEIN1 (PCaP1)[45] (Figure 7B-
389 7D), confirming previous protein-protein interaction studies. Interestingly, some of these proteins
390 did not meet the statistical threshold across all three pairwise comparisons. For instance, RIN4
391 was enriched in TbID-YFP-REM1.2 samples compared to the wild type under both control and
392 sorbitol conditions, but not in the direct comparison between the two conditions (Figure 7B-7D).
393 Similarly, PCaP1 was enriched in TbID-YFP-REM1.2 samples compared to the wild type under
394 sorbitol conditions, but not under control conditions; however, it was enriched in the comparison
395 between the two conditions (Figure 7B-7D). These findings raise the possibility of false

negatives in the pairwise comparisons described above and led us to test whether these proteins colocalize and interact with REM1.2 during hyperosmotic stress using an orthogonal approach. To this end, we performed confocal microscopy and FRET-FLIM analyses by transiently expressing YFP-REM1.2 in tobacco leaves, either alone or alongside an mRFP-tagged protein of interest. mRFP-REM1.3 served as a positive control, while free mRFP was used as a negative control. As anticipated, free mRFP localized to the cytosol did not colocalize with or interact with YFP-REM1.2 under either control or sorbitol treatment conditions (Figure 7E-7H). mRFP-REM1.3 colocalized and interacted with YFP-REM1.2 at the plasma membrane under control conditions and within nanodomains following sorbitol treatment (Figure 7E-7H). Similarly, mRFP-RIN4 and PCaP1-mRFP also exhibited colocalization and interaction with YFP-REM1.2 under both control and sorbitol conditions (Figure S7).

One group of proteins identified in the pairwise comparisons was the MECHANOSENSITIVE CHANNEL OF SMALL CONDUCTANCE-LIKEs (MSLs), including MSL4, MSL6, and MSL9 (Figure 7B-7D). In tobacco infiltration assays, mRFP-MSL4 and mRFP-MSL6 colocalized with YFP-REM1.2 at the plasma membrane under control conditions but not within nanodomains following sorbitol treatment (Figure S8A and S8B). However, under prolonged sorbitol treatment, colocalization was observed in the Hechtian reticulum (Figure S8A and S8B). In contrast, the localization pattern of mRFP-MSL9 resembled that of the cortical endoplasmic reticulum (ER) under both control and sorbitol conditions (Figure S8C), consistent with the close proximity of the ER to the plasma membrane where YFP-REM1.2 is located. This observation aligns with previous reports of MSL10, the closest homolog of MSL9 in the MSL family, being localized at ER-plasma membrane contact sites.[46,47] To assess the functional role of MSLs in Arabidopsis root growth responses to hyperosmotic stress, we compared the growth phenotypes of the *msl4;5;6;9;10* quintuple mutant and the wild type. However, no significant differences in growth were observed between the two genotypes under either control or sorbitol treatment conditions (Figure S8D), suggesting that none of these MSLs are required for root growth responses to hyperosmotic stress.

Another group of proteins identified in the pairwise comparisons was SHOU4/4L, known inhibitors of CSC exocytosis.[25] Similar to the positive control mRFP-REM1.3, both SHOU4-mRFP and SHOU4L-mRFP colocalized and interacted with YFP-REM1.2 at the plasma membrane under control conditions and within nanodomains following sorbitol treatment (Figure 7E-7H, Figure S9). In Arabidopsis roots, the *shou4-3 4l-1* double mutants displayed reduced root growth inhibition and increased resistance to plasmolysis than wild type under hyperosmotic stress (Figure 4G and 4H). These phenotypes closely resembled those of the *rem1.2 1.3 1.4* triple mutants (Figure 5F-5H). Together, these findings suggest that SHOU4/4L are components of the REM nanodomains that mediate the antagonism with CSC nanodomains.

Discussion

In summary, we provided genetic, live-cell imaging, and proximity labeling-based proteomic evidence that membrane nanodomains mediate the association and function of the cell wall-

440 plasma membrane interface. While these nanodomains are prominently observed at the outer
441 epidermal cell surface where they are in direct contact with the environment and function
442 independently of plasmodesmata, they are also likely present and functionally relevant at other
443 wall-membrane interfaces, such as in inner tissues where high-resolution live-cell imaging is
444 technically challenging. Maintaining CSC density at the plasma membrane is crucial for proper
445 cell wall-plasma membrane attachment and root responses to hyperosmotic stress. REMs
446 rapidly form nanodomains at the plasma membrane upon hyperosmotic stress and they harbor
447 many additional proteins in the vicinity, including the CSC exocytosis inhibitors SHOU4/4L.[25]
448 These findings reveal a molecular module in which CSCs are the core component that mediate
449 attachment between the cell wall and plasma membrane, acting downstream of and being
450 antagonized by REMs. Our findings provide new insights into the structural determinants of wall-
451 membrane attachment in plants and a physiological context in which their function supports the
452 resilience of plants to environmental stress.
453
454 Our survey of a panel of cell wall mutants in hyperosmotic stress-induced growth inhibition
455 revealed how different classes of cell wall polysaccharides are involved in this process. This
456 analysis led us to focus on two key proteins involved in cell wall biosynthesis: CSCs, and
457 RHM1. RHM1 encodes a UDP-L-rhamnose synthase, initially identified as a suppressor of
458 LEUCINE RICH REPEAT-EXTENSIN1 (LRX1), an extracellular protein that regulates cell wall
459 formation in root hairs.[48,49] RHM1 plays an important role in the morphogenesis of epidermal
460 cells, including root hairs,[48] cotyledon pavement cells,[50] and conical petal cells.[27,51] Although
461 rhamnose is required for both pectin biosynthesis and flavonol glycosylation, experimental
462 evidence suggests that rhamnose-containing RG-I directly contributes to epidermal
463 morphogenesis, whereas flavonol rhamnosylation has an indirect effect.[50,52] Our data reveal a
464 novel function of RHM1 in regulating root growth and responses to hyperosmotic stress (Figures
465 2 and 3). While we cannot definitively determine whether the observed *rhm1* mutant phenotypes
466 in our growth and plasmolysis assays result directly from RG-I rhamnose deficiency, we argue
467 that an indirect mechanism is more likely. This is supported by our findings that CSC machinery
468 components are enriched, and CSC density at the plasma membrane is increased, in the *rhm1-*
469 *1* mutant (Figure 3). Additionally, the *cesa3* mutation is epistatic to *rhm1-1* (Figure 4). These
470 findings underscore the intricate interplay among cell wall polymers:[7] altering one wall
471 component can influence the synthesis, assembly, and/or organization of others.[53–55]
472
473 Environmental changes influence CSC dynamics and cellulose synthesis.[56] For example, salt
474 stress reduces cellulose production and leads to CSC depletion and reappearance at the
475 plasma membrane that coincides with cortical microtubule reorganization,[57] a process requiring
476 COMPANION OF CELLULOSE SYNTHASE proteins[58] and TETRATRICOPEPTIDE
477 THIOREDOXIN-LIKE (TTL) proteins.[59] Treating Arabidopsis seedlings with hyperosmotic stress
478 for several hours, whether mild (200 mM mannitol) or moderate (500 mM mannitol), triggers the
479 redistribution of CSCs from the plasma membrane into small CESA compartments (SmaCCs)[38]
480 or microtubule-associated cellulose synthase compartments (MASCs).[60] Prolonged severe
481 osmotic stress has also been shown to reduce cellulose production.[61] In alignment with these
482 previous observations, we demonstrate that acute, severe osmotic stress causes a subset of
483 CSCs to remain at the plasma membrane, decorating Hechtian structures at cell wall-plasma

membrane attachment sites (Figure 4, Video S4). These CSCs are immobile (Figure S3, Video S3) and are likely inactive in cellulose synthesis, as CSC movement at the plasma membrane is thought to be driven by cellulose polymerization.[18] Additionally, our study establishes a functional link between CSC density at the plasma membrane and both root plasmolysis response at the cellular level and growth response at the organ level. These findings provide direct experimental evidence for the longstanding hypothesis that CSCs contribute to plasma membrane anchoring to the cell wall, perhaps through the nascent cellulose microfibril that is integrated into the cell wall.[19]

REMs, a plant-specific protein family,[62] are known to function in development,[40,43] plasmodesmata aperture regulation,[40] membrane topology stabilization in root nodule symbiosis,[23] and plant innate immunity.[63] Our work expands the understanding of REM function in environmental stress responses by demonstrating that the sterol-dependent (Figure S4), rapid formation of REM nanodomains at wall-membrane attachment sites (Figure 5, Video S5) upon hyperosmotic stress serves as a hub for the aggregation of many other proteins (Figures 7, S7, S8, and S9). In addition, we show that REMs act upstream of CSCs, with SHOU4/4L as their mediator, to regulate hyperosmotic stress responses in elongating roots (Figures 6 and 7). The elevated CSC density observed in *rem1.2 1.3 1.4* triple mutants (Figure 6) and in *shou4-3 4l-1* double mutants under non-stress conditions,[25] the unchanged CSC density following fenpropimorph treatment (Figure S5), along with the interaction between SHOU4/4L and REM1.2 in the absence of stress (Figures 7 and S9), suggests that REM-CSC antagonism occurs independently of REM nanodomain formation. This plasma membrane-localized molecular module, comprising CSCs, SHOU4/4L, and REMs, functions both as a structural anchor linking the cell wall to the plasma membrane and as a regulatory platform for coordinating hyperosmotic stress responses.

Limitations of the Study

The ultrastructural and organizational details of how CSCs mediate the physical association between the cell wall and plasma membrane remain to be elucidated. Although REM proteins were initially characterized for their ability to bind both simple and complex galacturonides *in vitro*,[24] it is still unclear whether such interactions occur *in vivo*. If they do, how REMs, peripheral proteins anchored to the inner leaflet of the plasma membrane, engage with cell wall pectins remains an open question. Our data revealed a correlation between plasmolysis upon hyperosmotic shock and growth inhibition under hyperosmotic stress, but the relationship between these two processes is not yet understood. In addition, proximity labeling identified numerous proteins in the vicinity of REM1.2, yet how these interactions change in response to hyperosmotic stress remains to be explored. These questions present exciting future directions that we aim to pursue through interdisciplinary approaches to advance our understanding of plant-environment interactions.

Acknowledgements

We thank past and present members of the Dinneny lab, Peter Dahlberg and his group at the SLAC National Accelerator Laboratory, the Plant Biology community at Stanford University, and Charles T. Anderson and his group at The Pennsylvania State University for insightful discussions and critical feedback. We are especially grateful to Andrea Mair and Dominique Bergmann for generously providing proximity labeling constructs and offering valuable advice on proximity labeling experiments. We thank Renate Weizbauer, Andrey Malkovskiy, and the Carnegie Advanced Imaging Facility for access to and assistance with the spinning disk confocal microscope. We also thank Daniel Miranda and Olivia Creasey for their help with 3D segmentation using AIVIA software. We gratefully acknowledge the following colleagues for sharing genetic materials: Siamsa Doyle and Stéphanie Robert for *mur2-1*, *mur3-1,* and *mur4-1* seeds; Olivier Hamant for *qua2-1* seeds; Henrik Scheller for *tbl10-1* and *gals1/2/3* seeds; Christoph Ringli for *RHM1-GFP*/*rhm1-2* seeds; Adam Saffer and Vivian Irish for *rhm1-3* seeds; Renee Weizbauer and David Ehrhardt for GFP-CESA3/mCherry-TUA5 seeds; Yvon Jaillais for mCherry-LTI6b seeds; Yoselin Benitez-Alfonso for mCherry-PDCB1 seeds; Xu Chen for *rem1.2 1.3c* seeds; and Charles T. Anderson for GFP-CESA3/tdTomato-CESA6 seeds.

Y.R. is a 2020 Simons fellow of the Life Sciences Research Foundation. This project was supported by grants awarded to J.R.D. from the Biological and Environmental Research (BER) Program, US Department of Energy (DE-AC02-76SF00515), National Institutes of Health, National Institute of General Medicine Sciences (R01 GM123259-01), the Stanford Precourt Institute, and a Faculty Scholars grant from the Simons Foundation and Howard Hughes Medical Institute (55108515), and a grant awarded to J.J.K. from the National Science Foundation (IOS-1856431). J.R.D. is an investigator of the Howard Hughes Medical Institute. N.B.A and T.O. were supported by the German Research Foundation (Deutsche Forschungsgemeinschaft; DFG) in frame of the Collaborative Research Center 924 (project ID 170483403). S.-L.X. was supported by the National Institutes of Health (S10OD030441) and the Carnegie endowment fund to the Carnegie mass spectrometry facility.

Author contributions

Conceptualization, Y.R. and J.R.D.; data acquisition and analysis, Y.R., A.V.R., T.S.G., N.B.A, W.P.D., and S.-L.X.; data interpretation, all authors; funding, Y.R., T.O., J.J.K., S.-L.X., and J.R.D; supervision, Y.R. and J.R.D; writing of the original draft, Y.R. and J.R.D; manuscript editing, Y.R., N.B.A, W.P.D., T.O., J.J.K., S.-L.X., and J.R.D..

Declaration of interests

The authors declare no competing interests.

Methods

Plant Materials and Growth

570 *Arabidopsis thaliana* seeds were surface-sterilized using a solution of 30% bleach and 0.1%
571 SDS for 20 minutes, followed by four rinses with sterile water. The sterilized seeds were
572 stratified in the dark at 4°C for 2-3 days before being germinated on 1X Murashige and Skoog
573 (MS) plates supplemented with 1% sucrose and solidified with 0.7% gelzan (pH 5.7). Seedlings
574 were grown vertically in a growth chamber maintained at 22°C under a 16-hour light/8-hour dark
575 photoperiod.
576
577 Molecular Cloning and Plant Transformation
578
579 The *CESA3* coding sequence with attB sites was amplified from Arabidopsis Col-0 cDNA and
580 introduced into the pDONR221 vector (Thermo Fisher, catalog #12536017) using a Gateway BP
581 reaction. A 1831-bp promoter fragment upstream of the *CESA3* start codon was amplified from
582 Col-0 genomic DNA with SbfI and XbaI restriction sites. The destination vector pGWB506
583 (Addgene, catalog #74848) was digested with SbfI and XbaI to replace the 35S promoter with
584 the *CESA3* promoter. The *CESA3* coding sequence was subsequently inserted into the
585 modified pGWB506 vector via a Gateway LR reaction to generate the *ProCESA3:GFP-CESA3*
586 construct. This construct was transformed into Arabidopsis Col-0 plants, and transgenic lines
587 were selected on medium containing 25 µg/mL Hygromycin B.
588
589 TurboID and YFP were amplified from the plasmid pENTR_L1-YFP-Turbo-L2 (Addgene, catalog
590 #127350). *LTI6b* was amplified from Col-0 genomic DNA, including its exons, introns, and
591 3'UTR. *REM1.2* was amplified from Col-0 cDNA. To generate TbID-YFP-LTI6b and TbID-YFP-
592 REM1.2, overlapping PCR was performed using these amplified fragments, introducing AgeI
593 and EcoRI restriction sites at the N- and C-termini, respectively. A 1568-bp promoter fragment
594 upstream of the *REM1.2* start codon was amplified from Col-0 genomic DNA, incorporating
595 PmeI and AgeI sites. The pEGAD empty vector (ABRC stock #CD3-389) was digested with
596 PmeI and AgeI to replace the *35S* promoter with the *REM1.2* promoter. This modified pEGAD
597 vector was subsequently digested with AgeI and EcoRI to replace the GFP sequence with TbID-
598 YFP-LTI6b or TbID-YFP-REM1.2. Constructs were then transformed into Arabidopsis Col-0 or
599 mutant backgrounds to generate transgenic lines, which were then selected using 50 µM Basta.
600
601 The *35S:YFP-REM1.2* construct used in tobacco infiltration assays was generated following the
602 same restriction digestion strategy described above. For *35S* promoter-driven mRFP-tagged
603 protein constructs, the coding sequences of *REM1.3*, *RIN4*, *PCaP1*, *SHOU4*, and *SHOU4L*
604 were amplified from Col-0 cDNA with attB sites. The genomic sequences of *MSL4*, *MSL6*, and
605 *MSL9*, including exons and introns, were amplified from Col-0 genomic DNA with attB sites. All
606 amplified sequences were first cloned into the pDONR221 vector and subsequently introduced
607 into pGWB554 (Addgene, catalog #74884) or pGWB555 (Addgene, catalog #74885) to create
608 mRFP fusion constructs with C- or N-terminal tags, respectively.
609
610 Root Growth Assay
611
612 Four-day-old seedlings grown on standard 1X MS media were transferred to either fresh
613 standard media or media supplemented with 0.28 M sorbitol. At the time of transfer, root tips

614 were marked to track growth. Seedlings were then grown for an additional day, after which the
615 plates were scanned using a dual-light flatbed scanner (Epson V800). Root growth was
616 quantified in ImageJ by measuring the root length extending beyond the marked position.
617
618 Pharmacological Treatments
619
620 To inhibit cellulose biosynthesis, we used isoxaben (ISX) (Sigma, catalog #36138-100MG) in
621 two different experimental setups. For acute clearance of CSCs from the plasma membrane,
622 five-day-old seedlings expressing GFP-LTI6b and tdTomato-CESA6 were incubated in MS
623 liquid containing 100 nM ISX for 20 min prior to imaging for plasmolysis. MS liquid with 0.1%
624 DMSO served as the mock treatment. To assess the effect of ISX on root growth, four-day-old
625 seedlings were transferred from standard 1X MS plates to one of four treatment conditions:
626 standard plates with 0.1% DMSO, standard plates with 1 nM ISX, 0.28 M sorbitol plates with
627 0.1% DMSO, or 0.28 M sorbitol plates with 1 nM ISX. Root growth was subsequently measured
628 as described above.
629
630 To inhibit sterol biosynthesis, 100 µg/mL fenpropimorph (Sigma, catalog #40713-100MG) was
631 added to standard 1X MS media. 1X MS media containing 0.1% DMSO was used as the mock.
632 Four-day-old seedlings expressing YFP-REM1.2 were transferred from standard plate to either
633 the mock or fenpropimorph plate and let grow for an additional day.
634
635 Confocal Microscopy
636
637 To visualize plasmolysis in transgenic lines expressing YFP- or GFP-LTI6b, five-day-old
638 seedlings were treated with 0.5 M sorbitol for 5 min on a glass slide and imaged on a Leica TCS
639 SP8 microscope with an HC PL APO 93x/1.3 NA objective. YFP was excited with a white light
640 laser at 514 nm, with emission detected between 525-570 nm. GFP was excited at 488 nm, with
641 emission detected between 500-560 nm. Bright-field and fluorescence images were acquired
642 simultaneously. The plasmolysis ratio was quantified in ImageJ by dividing the protoplast area
643 (measured from the fluorescence image) by the total cell area (measured from the bright-field
644 image). Protoplast curvature at cell ends was measured following previously established
645 methods.[64]
646
647 For calcofluor white staining, five-day-old seedlings were stained with 0.1 µM (10^{-5}%, w/v)
648 calcofluor white (Santa Cruz Biotechnology, catalog #sc-218504) diluted in MS liquid in the dark
649 for 30 min, washed with MS liquid, treated with fresh MS liquid or 1 M sorbitol for 5 min on a
650 glass slide, and imaged on a Leica TCS SP8 microscope with an HC PL APO 93x/1.3 NA
651 objective. Calcofluor was excited by UV at 405 nm, with emission detected between 420-470
652 nm.
653
654 CESA imaging was done on a Leica DMI6000 inverted microscope attached to a Yokogawa
655 spinning disk confocal head with a 100x/1.4 NA objective. GFP was excited at 488 nm with a
656 525/50 nm emission filter. tdTomato was excited at 561 nm with a 593/40 nm emission filter.
657 Excitation energy was adjusted to 4 mW power and exposure time was 200 ms. Z-stacks were

658 obtained with a step size of 0.27 µm. Time-lapse images were recorded at a single focal plane
659 at the plasma membrane with an interval of 10 s and a duration of 5 min.
660
661 REM imaging was performed using a Leica TCS SP8 microscope with an HC PL APO 93x/1.3
662 NA objective. YFP excitation and emission parameters were consistent with those described
663 above. For time-lapse imaging of REM nanodomain formation, a five-day-old YFP-REM1.2
664 seedling was placed under a 1X MS + 1% sucrose, 0.7% gelzan pad in a Nunc Lab-Tek
665 chambered coverglass (Thermo Fisher, catalog #155360). A 0.5-cm diameter hole was created
666 adjacent to the root tip. Time-lapse z-stack images were taken at a step-size of 0.3 µm,
667 beginning at 0 min (pre-treatment) and then every minute for 10 min following the addition of
668 200 µL of 0.5 M sorbitol into the hole. To image REM nanodomain disappearance upon relief
669 from hyperosmotic stress, a five-day-old YFP-REM1.2 seedling was pre-treated with 0.5 M
670 sorbitol for 5 min and then placed under a 1X MS + 1% sucrose + 0.5 M sorbitol, 0.7% gelzan
671 pad in a Nunc Lab-Tek chambered coverglass. Time-lapse z-stack imaging was performed
672 under the same parameters as described above, except that 200 µL of 1X MS + 1% sucrose
673 liquid solution was added to the hole instead of 0.5 M sorbitol.
674
675 Image Analysis
676
677 3D renderings of confocal images were generated using Leica LAS X or AIVIA 15.0.0 software
678 (Leica Microsystems). Hechtian structures were segmented in AIVIA. Quantitative image
679 analyses were performed with ImageJ and Imaris 10.1.1 (Oxford Instruments).
680
681 CESA density was quantified in ImageJ. Z-stack images were first background-subtracted using
682 the sliding paraboloid algorithm with a rolling ball radius of 30 pixels, and contrast was
683 enhanced by setting saturated pixels to 0.35%. For each root cell, a substack containing CESA
684 particles at the plasma membrane was generated and a maximum intensity projection was
685 created. A region of interest (ROI) was defined using the polygon tool to exclude the Golgi, and
686 its area was measured. Within this ROI, CESA particles were identified using the Find Maxima
687 tool with a noise tolerance of 500.
688
689 Time-lapse images of REM nanodomain formation and disappearance were processed in
690 ImageJ by generating maximum projections of z-stacks at each time point using ImageJ. The
691 resulting projections were concatenated and aligned using the StackReg plugin to correct for
692 frame shifts.
693
694 To measure REM nanodomain density, z-stack images were similarly contrast-enhanced in
695 ImageJ with saturated pixels set at 0.35%. A substack containing REM nanodomains at the
696 plasma membrane was generated for each root cell, followed by maximum intensity projection
697 and ROI selection using the polygon tool. The projection was then cropped and imported into
698 Imaris, where REM nanodomains were detected using a 0.4-µm diameter threshold.

699 Colocalization analysis for dual marker lines was performed in ImageJ using the Coloc 2 plugin.
700 For each root cell, an ROI was added to the ROI Manager and selected. Manders' overlap

701 coefficient was calculated using the Costes threshold regression method with 100 Costes
702 randomizations.

703 Biotin Treatment
704
705 One gram of five-day-old whole seedlings grown on MS plates was harvested into a nylon
706 biopsy bag (Fisher Scientific, catalog #50-303-41). The bag was submerged in either 50 μM
707 biotin in MS liquid medium (control) or 50 μM biotin in MS liquid supplemented with 0.5 M
708 sorbitol for 15 minutes. After treatment, samples were washed with the corresponding solution
709 (MS or MS + 0.5 M sorbitol) and gently blotted on a paper towel to remove excess liquid.
710 Samples were then flash-frozen in liquid nitrogen, ground into fine powder using a mortar and a
711 pestle, and stored at -80°C for further use.
712
713 Immunoblotting
714
715 To confirm biotinylation, 100 μl of finely ground frozen tissue powder from the biotin treatment
716 was resuspended in 100 μl of 2× Laemmli buffer containing 120 mM Tris (pH 6.8), 4% SDS,
717 20% glycerol, 5% β-mercaptoethanol, and 0.05% bromophenol blue. Samples were boiled at
718 95°C for 5 minutes, and 10 μl of the supernatant was loaded onto a 10% SDS-PAGE gel.
719 Proteins were transferred to a 0.2 μm PVDF membrane (Bio-Rad, catalog #1704156) using the
720 Trans-Blot Turbo Transfer System (Bio-Rad). Membranes were either stained with Coomassie
721 Brilliant Blue R-250 (Bio-Rad, catalog #1610400) for 30 seconds and destained with a solution
722 containing 40% methanol and 10% acetic acid, or blocked in 5% BSA in TBS and probed with
723 HRP-conjugated streptavidin (Thermo Fisher, catalog #S911) diluted 1:5,000 in 5% BSA in
724 TBST for 1 hour at room temperature. Chemiluminescence was detected using the Clarity ECL
725 Western Substrate (Bio-Rad, catalog #1705061) and visualized with the ChemiDoc MP Imaging
726 System (Bio-Rad).
727
728 Protein Affinity Purification
729
730 One gram of the finely ground frozen tissue powder from the biotin treatment was resuspended
731 in 2 mL of protein extraction buffer containing 50 mM Tris-HCl (pH 7.5), 150 mM NaCl, 0.1%
732 SDS, 1% Triton X-100, 0.5% sodium deoxycholate, 1 mM EGTA, 1 mM DTT, 1× cOmplete
733 protease inhibitor cocktail (Roche, catalog #COUEDTAF-RO), and 1 mM PMSF. The
734 suspension was vortexed and incubated on a rotor wheel at 4°C for 10 min. Samples were then
735 sonicated in an ice bath using a Branson 450 sonifier at 20% amplitude with 10 s on/10 s off
736 pulses for a total of 2 min. Following sonication, samples were centrifuged at 12,000 g for 10
737 min at 4°C. A total of 2.5 mL of the resulting supernatant was loaded onto PD-10 desalting
738 columns (Cytiva, catalog #17-0851-01) pre-equilibrated with equilibration buffer composed of 50
739 mM Tris-HCl (pH 7.5), 150 mM NaCl, 0.1% SDS, 1% Triton X-100, 0.5% sodium deoxycholate,
740 1 mM EGTA, and 1 mM DTT. Proteins were eluted with 3.5 mL of equilibration buffer into 5 mL
741 LoBind tubes (Eppendorf, catalog #0030108302). For streptavidin pulldown, 200 μL of
742 Dynabeads MyOne Streptavidin T1 beads (Thermo Fisher, catalog #65602) were washed with
743 extraction buffer and then incubated with the desalted protein extract supplemented with 1×

744 cOmplete protease inhibitor cocktail and 1 mM PMSF. The mixture was incubated overnight at
745 4°C on a rotor wheel. The following day, beads were separated using a magnetic rack,
746 transferred to 1.5 mL LoBind tubes (Eppendorf, catalog #022431081), and subjected to a series
747 of washes: twice with cold extraction buffer, twice with cold equilibration buffer, once with cold 1
748 M KCl, transferred to a fresh 1.5 mL LoBind tube, and washed twice more with cold extraction
749 buffer. After the final wash, beads were separated on a magnetic rack to remove residual buffer
750 and stored at -80°C for further use.
751
752 Mass Spectrometry Sample Preparation
753
754 Frozen streptavidin beads were thawed and washed once with PBS prepared in HPLC-grade
755 water (Thermo Fisher, catalog #022934-k7). The beads were transferred to a new 1.5 mL
756 LoBind tube and washed five additional times with PBS in HPLC-grade water. After the final
757 wash, beads were separated on a magnetic rack, and the buffer was carefully removed. Beads
758 were then incubated with 80 µL trypsin digestion buffer containing 50 mM Tris (pH 7.5), 1 M
759 Urea, 4 mM DTT, and 0.4 µg Trypsin at 25°C for 3 h with shaking at 1,200 rpm. Following
760 incubation, beads were magnetically separated and washed twice with 60 µL of 1 M urea in 50
761 mM Tris (pH 7.5). The resulting supernatants were pooled and treated with 10 mM
762 iodoacetamide at 25°C for 45 min in the dark with shaking at 1,200 rpm to alkylate cysteines.
763 Digestion was continued by adding 0.5 µg of additional trypsin, followed by overnight incubation
764 at 25°C with shaking at 1,200 rpm. The next day, a final 0.5 µg of trypsin was added, and
765 samples were incubated for an additional 4 h at 25°C with shaking. Following digestion, 1%
766 formic acid was added to acidify the samples, which were then vortexed and desalted using
767 OMIX C18 pipette tips (10-100 µL, Agilent, catalog #A57003100) according to the
768 manufacturer's instructions. Peptides were dried using a speed vacuum centrifuge and
769 resuspended in 0.1% formic acid for LC-MS/MS analysis. Samples were analyzed using a Q-
770 Exactive HF hybrid quadrupole-Orbitrap mass spectrometer (Thermo Fisher), coupled to an
771 Easy-nLC 1200 ultra-performance liquid chromatography system (Thermo Fisher).[29]
772
773 Mass Spectrometry Data Analysis
774
775 Mass spectrometry data were analyzed using MaxQuant (version 2.4.2.0)[65] and Perseus
776 (version 2.0.10.0)[66]. For plasma membrane proteome comparisons between wild type and
777 *cesa3*^{je5}, raw data from TbID-YFP-LTI6b/Col-0, Col-0, TbID-YFP-LTI6b/*cesa3*^{je5}, and *cesa3*^{je5}
778 were searched together in MaxQuant using default parameters with the following modifications.
779 The LFQ minimum ratio count was set to 2. Peptides were searched against the TAIR10 protein
780 database ("TAIR10_pep_20101214";
781 https://www.arabidopsis.org/download/list?dir=Proteins%2FTAIR10_protein_lists),
782 supplemented with a custom list of potential contaminants, such as trypsin, human keratin,
783 streptavidin, BSA, YFP, TbID-YFP, along with the standard MaxQuant contaminant list. "Match
784 between runs" was enabled with a match time window of 0.4 min and an alignment time window
785 of 20 min. The resulting "proteinGroups.txt" file was imported into Perseus with LFQ intensities
786 as the Main category. Proteins marked with reverse, contaminant, and only identified by site
787 identifications were removed. Data were log2-transformed, grouped, and filtered to retain

788 proteins with at least two valid values in at least one group. Data were imputed by replacing
789 missing LFQ values from normal distribution using the total matrix mode with a width of 0.3 and
790 down shift of 1.8. To remove all unspecific background labeling, each TbID-YFP-LTI6b-tagged
791 group was compared to its respective genetic background by a one-sided Welch's *t*-test with S0
792 of 0.5, FDR of 0.05, and 250 randomizations. The resulting filtered matrix was then used to
793 compare TbID-YFP-LTI6b/*cesa3*^{je5} and TbID-YFP-LTI6b/Col-0 using a two-sided Student's *t*-test
794 with S0 of 0.5, FDR of 0.05, and 250 randomizations.
795
796 The same workflow was applied to the plasma membrane proteome comparison between the
797 wild type and *rhm1-1*, using raw data of TbID-YFP-LTI6b/Col-0, Col-0, TbID-YFP-LTI6b/*rhm1-1*,
798 and *rhm1-1* samples.
799
800 For REM1.2 proximity labeling experiments, raw data from TbID-YFP-REM1.2/Col-0 (control
801 condition), TbID-YFP-LTI6b/Col-0 (control condition), Col-0 (control condition), TbID-YFP-
802 REM1.2/Col-0 (0.5 M sorbitol), TbID-YFP-LTI6b/Col-0 (0.5 M sorbitol), and Col-0 (0.5 M
803 sorbitol) were analyzed together using the same MaxQuant and Perseus workflow described
804 above. To remove background labeling, TbID-YFP-REM1.2/Col-0 was compared to Col-0 under
805 each condition by a one-sided Welch's *t*-test with S0 of 0.5, FDR of 0.05, and 250
806 randomizations. The resulting filtered matrix was then used to compare the 0.5 M sorbitol
807 treatment and the control condition in TbID-YFP-REM1.2/Col-0 using a two-sided Student's *t*-
808 test with S0 of 0.5, FDR of 0.05, and 250 randomizations.
809
810 The mass spectrometry proteomics data have been deposited to the ProteomeXchange
811 Consortium (http://proteomecentral.proteomexchange.org) via the PRIDE[67] partner repository.
812
813 Transient Expression in Tobacco
814
815 *Nicotiana benthamiana* seeds were sown directly in PRO-MIX HP soil and grown in a growth
816 chamber at 25°C under a 12-hour light/12-hour dark photoperiod. DNA constructs were
817 transformed into *Agrobacterium tumefaciens* GV3101 (pMP90 and pSoup) strain using
818 electroporation. Transformed Agrobacterium were cultured in 5 mL LB medium supplemented
819 with antibiotics for two days, then pelleted by centrifugation at 3,000 g for 10 minutes. Pellets
820 were resuspended and diluted in an infiltration medium containing 10 mM $MgCl_2$, 10 mM MES to
821 an OD600 of 0.5. Cultures were incubated at room temperature for 3 h with 150 µM
822 acetosyringone. For infiltration, cultures were mixed with the Agrobacterium p19 strain at an
823 OD600 of 0.2 and infiltrated to the abaxial side of leaves from 5- to 6-week-old Nicotiana plants.
824 Infiltrated plants were kept in the growth chamber for an additional 3-5 days before imaging.
825
826 FRET-FLIM
827
828 FRET-FLIM experiments in Nicotiana leaves were performed using a Leica TCS SP8 confocal
829 microscope equipped with an HC PL APO 93x/1.3 NA objective. Leaves infiltrated with YFP-
830 REM1.2 alone served as donor-only controls, while those co-infiltrated with YFP-REM1.2 and
831 an mRFP-tagged construct served as donor + acceptor samples. Samples were incubated in

832 either MS liquid medium or 1 M sorbitol to induce hyperosmotic stress. The donor (YFP) was
833 excited at 514 nm using a pulsed white light laser operating at 80 MHz. Emission was collected
834 between 525–570 nm using a HyD SMD hybrid detector. Laser power was adjusted to ensure a
835 maximum of approximately one photon per laser pulse, and frame repetition was set to 20.
836
837 YFP fluorescence lifetimes were measured using the LAS X software. Under control conditions,
838 ROIs were defined as narrow rectangular areas along the plasma membrane at cell borders.
839 Under hyperosmotic stress, ROIs were selected based on individual YFP-REM1.2
840 nanodomains. Approximately 3-5 ROIs were analyzed per image. YFP lifetimes were calculated
841 using an n-Exponential Reconvolution model with one component.
842
843 Quantification and Statistical Analysis
844
845 Grouped and scattered column graphs displaying mean ± SD were generated using Prism 10
846 (GraphPad). Histograms were created in Microsoft Excel, and volcano plots were generated
847 using R. Statistical analyses were performed using two-way ANOVA in Prism 10. Details of
848 statistical tests, including sample sizes and significance levels, are provided in the figures and
849 corresponding legends.
850
851 **References**

852 1. Theocharis, A.D., Skandalis, S.S., Gialeli, C., and Karamanos, N.K. (2016). Extracellular
853 matrix structure. Adv. Drug Deliv. Rev. *97*, 4–27.

854 2. Humphries, J.D., Byron, A., and Humphries, M.J. (2006). Integrin ligands at a glance. J.
855 Cell Sci. *119*, 3901–3903.

856 3. Kohorn, B.D. (2000). Plasma membrane-cell wall contacts. Plant Physiol. *124*, 31–38.

857 4. Feng, W., Lindner, H., Robbins, N.E., 2nd, and Dinneny, J.R. (2016). Growing Out of
858 Stress: The Role of Cell- and Organ-Scale Growth Control in Plant Water-Stress
859 Responses. Plant Cell *28*, 1769–1782.

860 5. Lampugnani, E.R., Khan, G.A., Somssich, M., and Persson, S. (2018). Building a plant cell
861 wall at a glance. J. Cell Sci. *131*. https://doi.org/10.1242/jcs.207373.

862 6. Delmer, D., Dixon, R.A., Keegstra, K., and Mohnen, D. (2024). The plant cell wall-dynamic,
863 strong, and adaptable-is a natural shapeshifter. Plant Cell *36*, 1257–1311.

864 7. Rui, Y., and Dinneny, J.R. (2020). A wall with integrity: surveillance and maintenance of the
865 plant cell wall under stress. New Phytol. *225*, 1428–1439.

866 8. Martinière, A., Lavagi, I., Nageswaran, G., Rolfe, D.J., Maneta-Peyret, L., Luu, D.-T.,
867 Botchway, S.W., Webb, S.E.D., Mongrand, S., Maurel, C., et al. (2012). Cell wall constrains
868 lateral diffusion of plant plasma-membrane proteins. Proc. Natl. Acad. Sci. U. S. A. *109*,
869 12805–12810.

870 9. McKenna, J.F., Rolfe, D.J., Webb, S.E.D., Tolmie, A.F., Botchway, S.W., Martin-
871 Fernandez, M.L., Hawes, C., and Runions, J. (2019). The cell wall regulates dynamics and

872 size of plasma-membrane nanodomains in Arabidopsis. Proc. Natl. Acad. Sci. U. S. A. *116*,
873 12857–12862.

874 10. Jaillais, Y., Bayer, E., Bergmann, D.C., Botella, M.A., Boutté, Y., Bozkurt, T.O., Caillaud,
875 M.-C., Germain, V., Grossmann, G., Heilmann, I., et al. (2024). Guidelines for naming and
876 studying plasma membrane domains in plants. Nat. Plants *10*, 1172–1183.

877 11. Hdedeh, O., Mercier, C., Poitout, A., Martinière, A., and Zelazny, E. (2025). Membrane
878 nanodomains to shape plant cellular functions and signaling. New Phytol. *245*, 1369–1385.

879 12. Feng, W., Kita, D., Peaucelle, A., Cartwright, H.N., Doan, V., Duan, Q., Liu, M.-C., Maman,
880 J., Steinhorst, L., Schmitz-Thom, I., et al. (2018). The FERONIA Receptor Kinase Maintains
881 Cell-Wall Integrity during Salt Stress through Ca2+ Signaling. Curr. Biol. *28*, 666–675.e5.

882 13. Hecht., V.K. (1912). Studien über den Vorgang der Plasmolyse (Beitr. Biol. Pflanz.).

883 14. Arico, D.S., Dickmann, J.E.M., Hamant, O., and Canut, H. (2023). The plasma membrane -
884 cell wall nexus in plant cells: focus on the Hechtian structure. Cell Surf. *10*, 100115.

885 15. Haswell, E.S., and Verslues, P.E. (2015). The ongoing search for the molecular basis of
886 plant osmosensing. J. Gen. Physiol. *145*, 389–394.

887 16. Yu, Q., Ren, J.-J., Kong, L.-J., and Wang, X.-L. (2018). Actin filaments regulate the
888 adhesion between the plasma membrane and the cell wall of tobacco guard cells.
889 Protoplasma *255*, 235–245.

890 17. Gronnier, J., Gerbeau-Pissot, P., Germain, V., Mongrand, S., and Simon-Plas, F. (2018).
891 Divide and Rule: Plant Plasma Membrane Organization. Trends Plant Sci. *23*, 899–917.

892 18. Paredez, A.R., Somerville, C.R., and Ehrhardt, D.W. (2006). Visualization of cellulose
893 synthase demonstrates functional association with microtubules. Science *312*, 1491–1495.

894 19. Lang, I., Barton, D.A., and Overall, R.L. (2004). Membrane-wall attachments in
895 plasmolysed plant cells. Protoplasma *224*, 231–243.

896 20. Smokvarska, M., Francis, C., Platre, M.P., Fiche, J.-B., Alcon, C., Dumont, X., Nacry, P.,
897 Bayle, V., Nollmann, M., Maurel, C., et al. (2020). A plasma membrane nanodomain
898 ensures signal specificity during osmotic signaling in plants. Curr. Biol. *30*, 4654–4664.e4.

899 21. Gouguet, P., Gronnier, J., Legrand, A., Perraki, A., Jolivet, M.-D., Deroubaix, A.-F.,
900 German-Retana, S., Boudsocq, M., Habenstein, B., Mongrand, S., et al. (2021). Connecting
901 the dots: from nanodomains to physiological functions of REMORINs. Plant Physiol. *185*,
902 632–649.

903 22. Liang, P., Stratil, T.F., Popp, C., Marín, M., Folgmann, J., Mysore, K.S., Wen, J., and Ott, T.
904 (2018). Symbiotic root infections in Medicago truncatula require remorin-mediated receptor
905 stabilization in membrane nanodomains. Proc. Natl. Acad. Sci. U. S. A. *115*, 5289–5294.

906 23. Su, C., Rodriguez-Franco, M., Lace, B., Nebel, N., Hernandez-Reyes, C., Liang, P.,
907 Schulze, E., Mymrikov, E.V., Gross, N.M., Knerr, J., et al. (2023). Stabilization of
908 membrane topologies by proteinaceous remorin scaffolds. Nat. Commun. *14*, 323.

909 24. Reymond, P., Kunz, B., Paul-Pletzer, K., Grimm, R., Eckerskorn, C., and Farmer, E.E.

910 (1996). Cloning of a cDNA encoding a plasma membrane-associated, uronide binding
911 phosphoprotein with physical properties similar to viral movement proteins. Plant Cell *8*,
912 2265–2276.

913 25. Polko, J.K., Barnes, W.J., Voiniciuc, C., Doctor, S., Steinwand, B., Hill, J.L., Jr, Tien, M.,
914 Pauly, M., Anderson, C.T., and Kieber, J.J. (2018). SHOU4 proteins regulate trafficking of
915 cellulose synthase complexes to the plasma membrane. Curr. Biol. *28*, 3174–3182.e6.

916 26. Mouille, G., Ralet, M.-C., Cavelier, C., Eland, C., Effroy, D., Hématy, K., McCartney, L.,
917 Truong, H.N., Gaudon, V., Thibault, J.-F., et al. (2007). Homogalacturonan synthesis in
918 Arabidopsis thaliana requires a Golgi-localized protein with a putative methyltransferase
919 domain: Homogalacturonan synthesis in Arabidopsis: Plant J. *50*, 605–614.

920 27. Saffer, A.M., Carpita, N.C., and Irish, V.F. (2017). Rhamnose-Containing Cell Wall
921 Polymers Suppress Helical Plant Growth Independently of Microtubule Orientation. Curr.
922 Biol. *27*, 2248–2259.e4.

923 28. Ebert, B., Birdseye, D., Liwanag, A.J.M., Laursen, T., Rennie, E.A., Guo, X., Catena, M.,
924 Rautengarten, C., Stonebloom, S.H., Gluza, P., et al. (2018). The three members of the
925 Arabidopsis Glycosyltransferase Family 92 are functional β-1,4-galactan synthases. Plant
926 Cell Physiol. *59*, 2624–2636.

927 29. Mair, A., Xu, S.-L., Branon, T.C., Ting, A.Y., and Bergmann, D.C. (2019). Proximity labeling
928 of protein complexes and cell-type-specific organellar proteomes in Arabidopsis enabled by
929 TurboID. Elife *8*, e47864.

930 30. Xu, S.-L., Shrestha, R., Karunadasa, S.S., and Xie, P.-Q. (2023). Proximity labeling in
931 plants. Annu. Rev. Plant Biol. *74*, 285–312.

932 31. Moulinier-Anzola, J., De-Araujo, L., and Korbei, B. (2014). Expression of Arabidopsis TOL
933 genes. Plant Signal. Behav. *9*, e28667.

934 32. Korbei, B., Moulinier-Anzola, J., De-Araujo, L., Lucyshyn, D., Retzer, K., Khan, M.A., and
935 Luschnig, C. (2013). Arabidopsis TOL proteins act as gatekeepers for vacuolar sorting of
936 PIN2 plasma membrane protein. Curr. Biol. *23*, 2500–2505.

937 33. Li, S., Lei, L., Somerville, C.R., and Gu, Y. (2012). Cellulose synthase interactive protein 1
938 (CSI1) links microtubules and cellulose synthase complexes. Proc. Natl. Acad. Sci. U. S. A.
939 *109*, 185–190.

940 34. Bringmann, M., Li, E., Sampathkumar, A., Kocabek, T., Hauser, M.-T., and Persson, S.
941 (2012). POM-POM2/cellulose synthase interacting1 is essential for the functional
942 association of cellulose synthase and microtubules in Arabidopsis. Plant Cell *24*, 163–177.

943 35. Lei, L., Li, S., Du, J., Bashline, L., and Gu, Y. (2013). Cellulose synthase INTERACTIVE3
944 regulates cellulose biosynthesis in both a microtubule-dependent and microtubule-
945 independent manner in Arabidopsis. Plant Cell *25*, 4912–4923.

946 36. Zhu, X., Li, S., Pan, S., Xin, X., and Gu, Y. (2018). CSI1, PATROL1, and exocyst complex
947 cooperate in delivery of cellulose synthase complexes to the plasma membrane. Proc. Natl.
948 Acad. Sci. U. S. A. *115*, E3578–E3587.

949 37. Liu, Z., Schneider, R., Kesten, C., Zhang, Y., Somssich, M., Zhang, Y., Fernie, A.R., and
950 Persson, S. (2016). Cellulose-microtubule uncoupling proteins prevent lateral displacement
951 of microtubules during cellulose synthesis in Arabidopsis. Dev. Cell *38*, 305–315.

952 38. Gutierrez, R., Lindeboom, J.J., Paredez, A.R., Emons, A.M.C., and Ehrhardt, D.W. (2009).
953 Arabidopsis cortical microtubules position cellulose synthase delivery to the plasma
954 membrane and interact with cellulose synthase trafficking compartments. Nat. Cell Biol. *11*,
955 797–806.

956 39. Gronnier, J., Crowet, J.-M., Habenstein, B., Nasir, M.N., Bayle, V., Hosy, E., Platre, M.P.,
957 Gouguet, P., Raffaele, S., Martinez, D., et al. (2017). Structural basis for plant plasma
958 membrane protein dynamics and organization into functional nanodomains. Elife *6*, e26404.

959 40. Huang, D., Sun, Y., Ma, Z., Ke, M., Cui, Y., Chen, Z., Chen, C., Ji, C., Tran, T.M., Yang, L.,
960 et al. (2019). Salicylic acid-mediated plasmodesmal closure via Remorin-dependent lipid
961 organization. Preprint, https://doi.org/10.1073/pnas.1911892116
962 https://doi.org/10.1073/pnas.1911892116.

963 41. Benitez-Alfonso, Y., Faulkner, C., Pendle, A., Miyashima, S., Helariutta, Y., and Maule, A.
964 (2013). Symplastic intercellular connectivity regulates lateral root patterning. Dev. Cell *26*,
965 136–147.

966 42. Grison, M.S., Kirk, P., Brault, M.L., Wu, X.N., Schulze, W.X., Benitez-Alfonso, Y., Immel, F.,
967 and Bayer, E.M. (2019). Plasma Membrane-Associated Receptor-like Kinases Relocalize to
968 Plasmodesmata in Response to Osmotic Stress. Plant Physiol. *181*, 142–160.

969 43. Abel, N.B., Buschle, C.A., Hernandez-Ryes, C., Burkart, S.S., Deroubaix, A.-F., Mergner,
970 J., Gronnier, J., Jarsch, I.K., Folgmann, J., Braun, K.H., et al. (2021). A hetero-oligomeric
971 remorin-receptor complex regulates plant development. bioRxiv, 2021.01.28.428596.
972 https://doi.org/10.1101/2021.01.28.428596.

973 44. Liu, J., Elmore, J.M., and Coaker, G. (2009). Investigating the functions of the RIN4 protein
974 complex during plant innate immune responses. Plant Signal. Behav. *4*, 1107–1110.

975 45. Cheng, G., Yang, Z., Zhang, H., Zhang, J., and Xu, J. (2020). Remorin interacting with
976 PCaP1 impairs Turnip mosaic virus intercellular movement but is antagonised by VPg. New
977 Phytol. *225*, 2122–2139.

978 46. Codjoe, J.M., Richardson, R.A., McLoughlin, F., Vierstra, R.D., and Haswell, E.S. (2022).
979 Unbiased proteomic and forward genetic screens reveal that mechanosensitive ion channel
980 MSL10 functions at ER-plasma membrane contact sites in Arabidopsis thaliana. Elife *11*,
981 e80501.

982 47. Haswell, E.S., Peyronnet, R., Barbier-Brygoo, H., Meyerowitz, E.M., and Frachisse, J.-M.
983 (2008). Two MscS homologs provide mechanosensitive channel activities in the
984 Arabidopsis root. Curr. Biol. *18*, 730–734.

985 48. Diet, A., Link, B., Seifert, G.J., Schellenberg, B., Wagner, U., Pauly, M., Reiter, W.-D., and
986 Ringli, C. (2006). The Arabidopsis root hair cell wall formation mutant lrx1 is suppressed by
987 mutations in the RHM1 gene encoding a UDP-L-rhamnose synthase. Plant Cell *18*, 1630–
988 1641.

989 49. Baumberger, N., Ringli, C., and Keller, B. (2001). The chimeric leucine-rich repeat/extensin
990 cell wall protein LRX1 is required for root hair morphogenesis in Arabidopsis thaliana.
991 Genes Dev. *15*, 1128–1139.

992 50. Ringli, C., Bigler, L., Kuhn, B.M., Leiber, R.-M., Diet, A., Santelia, D., Frey, B., Pollmann, S.,
993 and Klein, M. (2008). The modified flavonol glycosylation profile in the Arabidopsis rol1
994 mutants results in alterations in plant growth and cell shape formation. Plant Cell *20*, 1470–
995 1481.

996 51. Field, S., Dorone, Y., Dwyer, W.P., Cox, J.A., Raba, D., Froehlich, J., Blea, M., Carmo,
997 O.M.S., Wallace, I.S., Hastings, R., et al. (2024). Arabidopsis thaliana RHAMNOSE 1
998 condensate formation drives UDP-rhamnose synthesis. bioRxivorg.
999 https://doi.org/10.1101/2024.02.15.580454.

1000 52. Saffer, A.M., and Irish, V.F. (2018). Flavonol rhamnosylation indirectly modifies the cell wall
1001 defects of RHAMNOSE BIOSYNTHESIS1 mutants by altering rhamnose flux. Plant J. *94*,
1002 649–660.

1003 53. Xiao, C., Zhang, T., Zheng, Y., Cosgrove, D.J., and Anderson, C.T. (2016). Xyloglucan
1004 deficiency disrupts microtubule stability and cellulose biosynthesis in Arabidopsis, altering
1005 cell growth and morphogenesis. Plant Physiol. *170*, 234–249.

1006 54. Du, J., Kirui, A., Huang, S., Wang, L., Barnes, W.J., Kiemle, S.N., Zheng, Y., Rui, Y., Ruan,
1007 M., Qi, S., et al. (2020). Mutations in the pectin methyltransferase QUASIMODO2 influence
1008 cellulose biosynthesis and wall integrity in Arabidopsis. Plant Cell *32*, 3576–3597.

1009 55. Saffer, A.M., Baskin, T.I., Verma, A., Stanislas, T., Oldenbourg, R., and Irish, V.F. (2023).
1010 Cellulose assembles into helical bundles of uniform handedness in cell walls with abnormal
1011 pectin composition. Plant J. *116*, 855–870.

1012 56. Wang, T., McFarlane, H.E., and Persson, S. (2016). The impact of abiotic factors on
1013 cellulose synthesis. J. Exp. Bot. *67*, 543–552.

1014 57. Wang, C., Li, J., and Yuan, M. (2007). Salt tolerance requires cortical microtubule
1015 reorganization in Arabidopsis. Plant Cell Physiol. *48*, 1534–1547.

1016 58. Endler, A., Kesten, C., Schneider, R., Zhang, Y., Ivakov, A., Froehlich, A., Funke, N., and
1017 Persson, S. (2015). A Mechanism for Sustained Cellulose Synthesis during Salt Stress.
1018 Cell *162*, 1353–1364.

1019 59. Kesten, C., García-Moreno, Á., Amorim-Silva, V., Menna, A., Castillo, A.G., Percio, F.,
1020 Armengot, L., Ruiz-Lopez, N., Jaillais, Y., Sánchez-Rodríguez, C., et al. (2022). Peripheral
1021 membrane proteins modulate stress tolerance by safeguarding cellulose synthases. Sci.
1022 Adv. *8*, eabq6971.

1023 60. Crowell, E.F., Bischoff, V., Desprez, T., Rolland, A., Stierhof, Y.-D., Schumacher, K.,
1024 Gonneau, M., Höfte, H., and Vernhettes, S. (2009). Pausing of Golgi bodies on
1025 microtubules regulates secretion of cellulose synthase complexes in Arabidopsis. Plant Cell
1026 *21*, 1141–1154.

1027 61. Iraki, N.M., Bressan, R.A., Hasegawa, P.M., and Carpita, N.C. (1989). Alteration of the
1028 physical and chemical structure of the primary cell wall of growth-limited plant cells adapted

1029 to osmotic stress. Plant Physiol. *91*, 39–47.

1030 62. Raffaele, S., Mongrand, S., Gamas, P., Niebel, A., and Ott, T. (2007). Genome-wide
1031 annotation of remorins, a plant-specific protein family: evolutionary and functional
1032 perspectives. Plant Physiol. *145*, 593–600.

1033 63. Ma, Z., Sun, Y., Zhu, X., Yang, L., Chen, X., and Miao, Y. (2022). Membrane nanodomains
1034 modulate formin condensation for actin remodeling in Arabidopsis innate immune
1035 responses. Plant Cell *34*, 374–394.

1036 64. Segev-Zarko, L.-A., Dahlberg, P.D., Sun, S.Y., Pelt, D.M., Kim, C.Y., Egan, E.S., Sethian,
1037 J.A., Chiu, W., and Boothroyd, J.C. (2022). Cryo-electron tomography with mixed-scale
1038 dense neural networks reveals key steps in deployment of Toxoplasma invasion machinery.
1039 PNAS Nexus *1*, gac183.

1040 65. Tyanova, S., Temu, T., and Cox, J. (2016). The MaxQuant computational platform for mass
1041 spectrometry-based shotgun proteomics. Nat. Protoc. *11*, 2301–2319.

1042 66. Tyanova, S., Temu, T., Sinitcyn, P., Carlson, A., Hein, M.Y., Geiger, T., Mann, M., and Cox,
1043 J. (2016). The Perseus computational platform for comprehensive analysis of (prote)omics
1044 data. Nat. Methods *13*, 731–740.

1045 67. Vizcaíno, J.A., Côté, R.G., Csordas, A., Dianes, J.A., Fabregat, A., Foster, J.M., Griss, J.,
1046 Alpi, E., Birim, M., Contell, J., et al. (2013). The PRoteomics IDEntifications (PRIDE)
1047 database and associated tools: status in 2013. Nucleic Acids Res. *41*, D1063–D1069.

1048

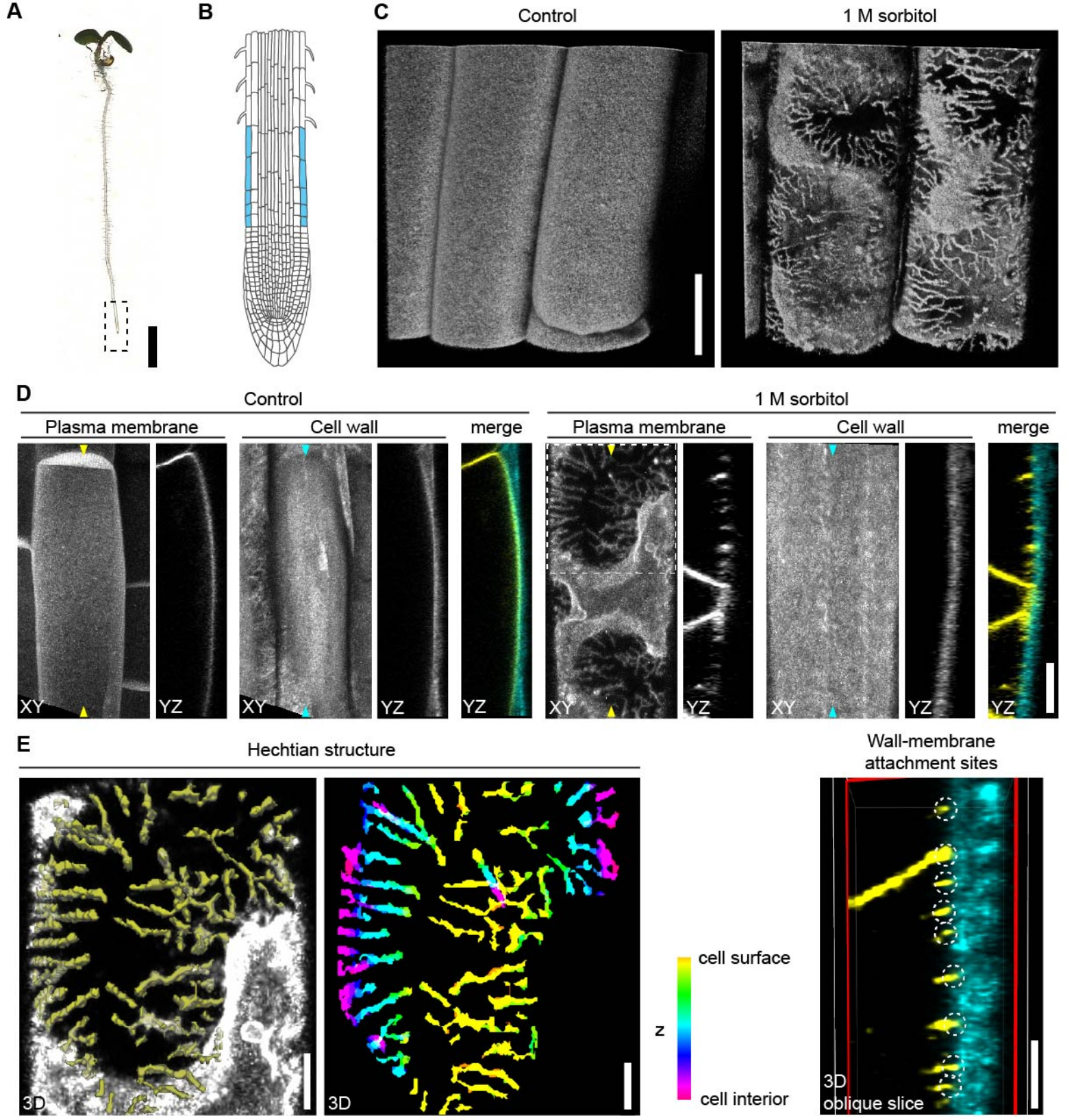
A
B
C
Control
1 M sorbitol
D
Control
1 M sorbitol
Plasma membrane
Cell wall
merge
Plasma membrane
Cell wall
merge
XY
YZ
XY
YZ
YZ
XY
YZ
XY
YZ
YZ
E
Hechtian structure
Wall-membrane attachment sites
3D
3D
cell surface
z
cell interior
3D
oblique slice

Figure 1. Hyperosmotic stress reveals cell wall-plasma membrane attachment sites in Arabidopsis roots.

(A) A 5-d-old Arabidopsis seedling grown on MS media. Box demarcates the root tip. Scale bar: 0.2 cm.

(B) Diagram of the longitudinal section of an Arabidopsis root tip in (A). Epidermal cells in the elongation zone are color coded in blue, which represent the regions where images in (C) were taken.

(C) 3D rendering of root epidermal cells in 5-d-old seedlings expressing a plasma membrane marker, YFP-LTI6b, under the control condition or treated with 1 M sorbitol for 5 min. Scale bar: 10 μm.

(D) Laser scanning confocal images of root epidermal cells from 5-day-old seedlings expressing the plasma membrane marker YFP-LTI6b and co-stained with the cell wall dye calcofluor white. Seedlings were imaged under control conditions or after treatment with 1 M sorbitol for 5 min. XY and YZ projections are shown. The positions where YZ projections were made are indicated by arrowheads. Scale bar: 5 μm.

(E) 3D segmentation of Hechtian structure and wall-membrane attachment sites from the dashed box region in (D). Segmented Hechtian structure is shown either in yellow, overlaid on YFP-LTI6b signals, or with depth-based color coding. Wall-membrane attachment sites (indicated by white dashed circles) are visualized by applying an oblique slicer (outlined in red) to the YZ projection. Scale bars: 2 μm. See also Video S1.

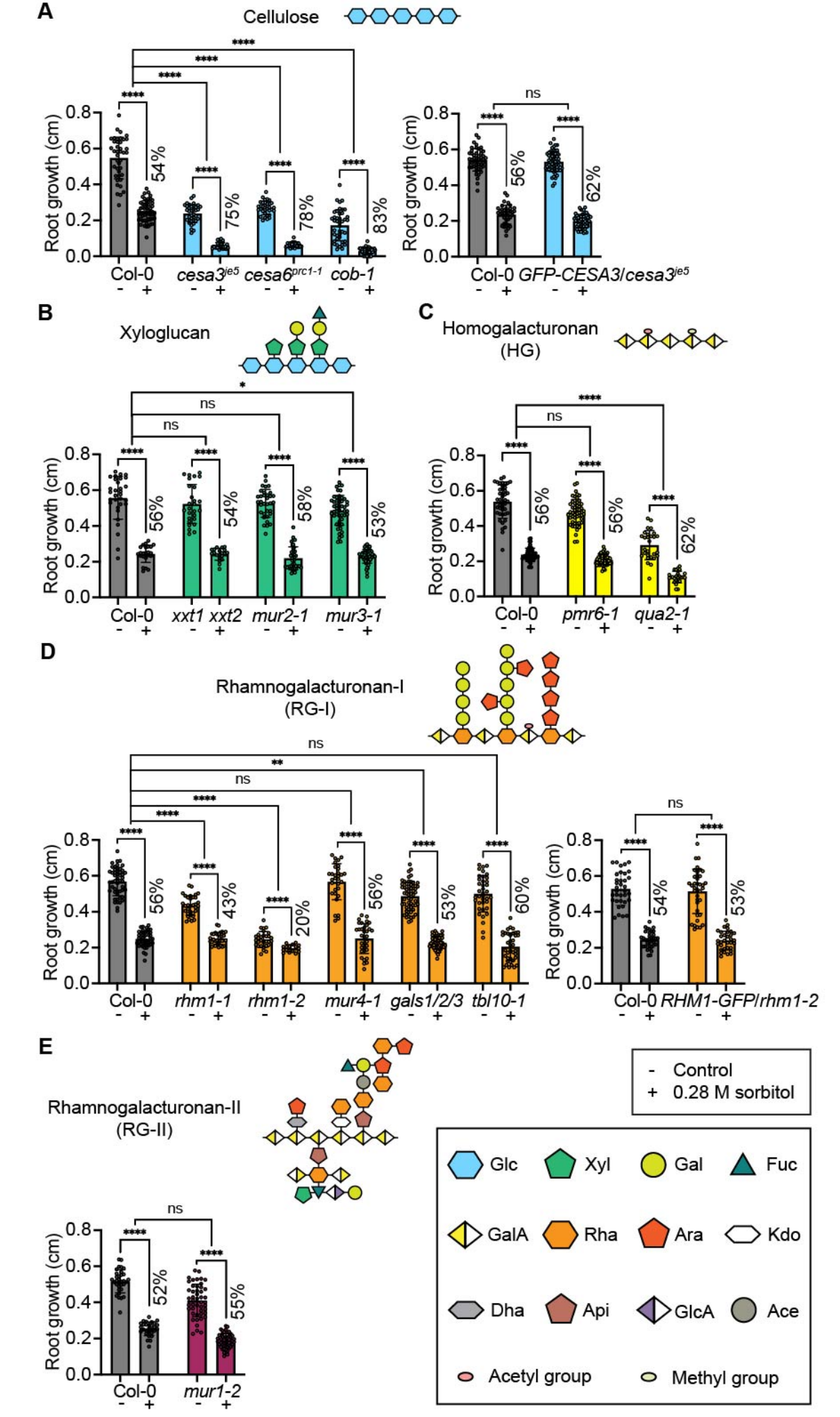
A
Cellulose
Root growth (cm)
54%
75%
78%
83%
Col-0
cesa3je5
cesa6prc1-1
cob-1
ns
56%
62%
GFP-CESA3/cesa3je5
B
Xyloglucan
56%
54%
58%
53%
xxt1 xxt2
mur2-1
mur3-1
C
Homogalacturonan
(HG)
56%
56%
62%
pmr6-1
qua2-1
D
Rhamnogalacturonan-I
(RG-I)
56%
43%
20%
56%
53%
60%
rhm1-1
rhm1-2
mur4-1
gals1/2/3
tbl10-1
54%
53%
RHM1-GFP/rhm1-2
E
Rhamnogalacturonan-II
(RG-II)
52%
55%
mur1-2
- Control
+ 0.28 M sorbitol
Glc
Xyl
Gal
Fuc
GalA
Rha
Ara
Kdo
Dha
Api
GlcA
Ace
Acetyl group
Methyl group

Figure 2. Reductions in cellulose and rhamnose impact root growth under hyperosmotic stress in opposing ways.

(A) Root growth of wild type, cellulose-deficient mutants, and a *CESA3* complementation line 1 day after transfer to either fresh MS media (-) or MS media supplemented with 0.28 M sorbitol (+). $n \geq 27$ seedlings per genotype per treatment.

(B) Root growth of wild type and xyloglucan mutants 1 day after transfer to either fresh MS media (-) or MS media supplemented with 0.28 M sorbitol (+). $n \geq 20$ seedlings per genotype per treatment.

(C) Root growth of wild type and homogalacturonan mutants 1 day after transfer to either fresh MS media (-) or MS media supplemented with 0.28 M sorbitol (+). $n \geq 25$ seedlings per genotype per treatment.

(D) Root growth of wild type and rhamnogalacturonan-I mutants 1 day after transfer to either fresh MS media (-) or MS media supplemented with 0.28 M sorbitol (+). $n \geq 16$ seedlings per genotype per treatment.

(E) Root growth of wild type and rhamnogalacturonan-II mutants 1 day after transfer to either fresh MS media (-) or MS media supplemented with 0.28 M sorbitol (+). $n \geq 29$ seedlings per genotype per treatment.

Error bars indicate SD. ns, no significance; $^{*}p < 0.05$, $^{**}p < 0.01$, $^{***}p < 0.001$, $^{****}p < 0.0001$ by two-way ANOVA.

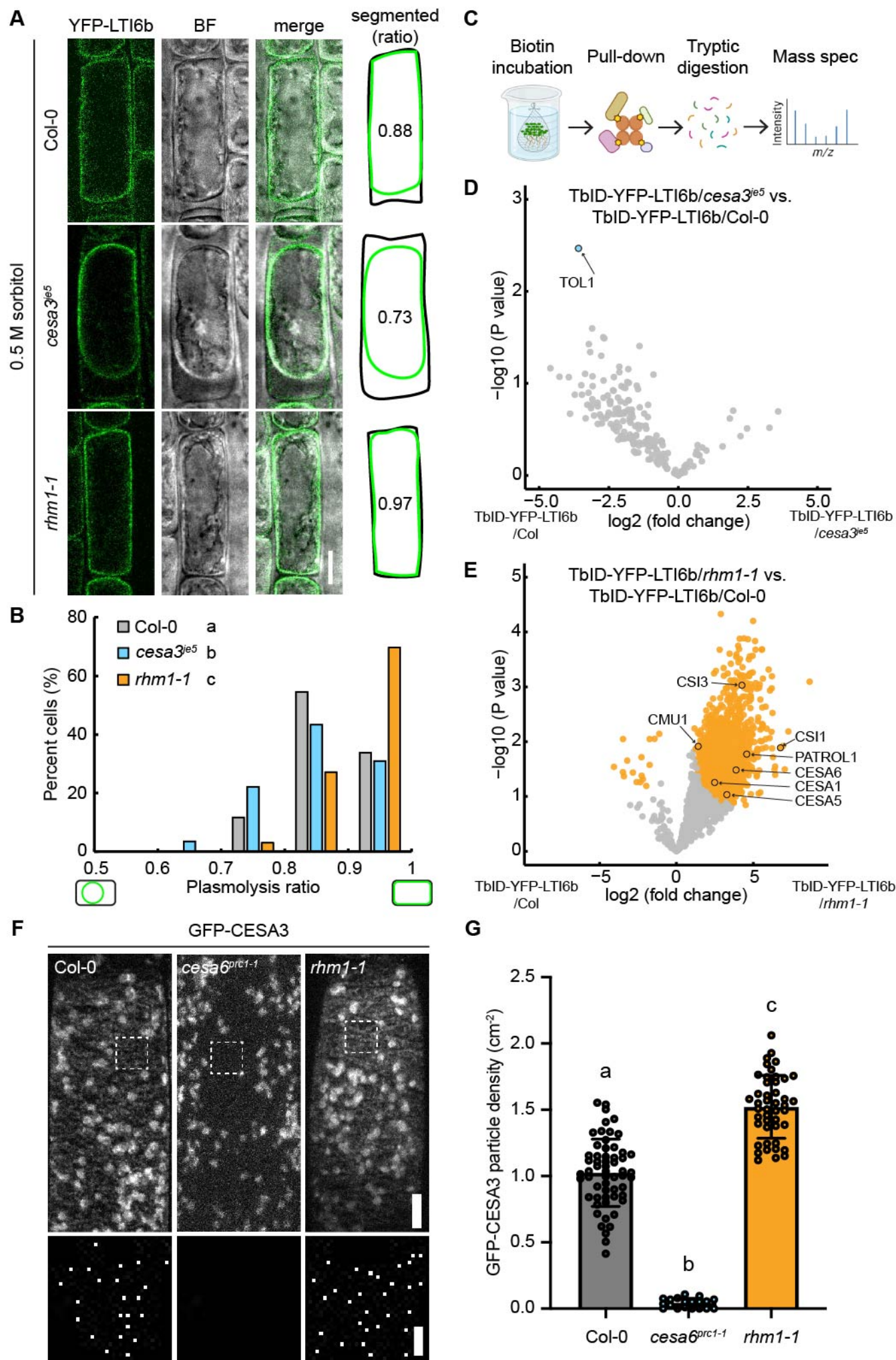
A
YFP-LTI6b
BF
merge
segmented (ratio)
0.5 M sorbitol
Col-0
cesa3^ie5
rhm1-1
0.88
0.73
0.97
B
Col-0 a
cesa3^ie5 b
rhm1-1 c
Percent cells (%)
Plasmolysis ratio
C
Biotin incubation
Pull-down
Tryptic digestion
Mass spec
Intensity
m/z
D
TbID-YFP-LTI6b/cesa3^ie5 vs. TbID-YFP-LTI6b/Col-0
TOL1
−log10 (P value)
log2 (fold change)
TbID-YFP-LTI6b /Col
TbID-YFP-LTI6b /cesa3^ie5
E
TbID-YFP-LTI6b/rhm1-1 vs. TbID-YFP-LTI6b/Col-0
CSI3
CMU1
CSI1
PATROL1
CESA6
CESA1
CESA5
−log10 (P value)
log2 (fold change)
TbID-YFP-LTI6b /Col
TbID-YFP-LTI6b /rhm1-1
F
GFP-CESA3
Col-0
cesa6^prc1-1
rhm1-1
G
GFP-CESA3 particle density (cm^-2)
a
b
c
Col-0
cesa6^prc1-1
rhm1-1

Figure 3. Deficiency in cellulose or rhamnose has opposite effects on plasmolysis and the plasma membrane proteome.

(A) Laser scanning confocal images and manual tracings of plasmolyzed root epidermal cells in 5-d-old seedlings expressing YFP-LTI6b in Col-0, *cesa3*^{je5}, or *rhm1-1* background, respectively. Plasmolysis was induced by 0.5 M sorbitol for 5 min. Each displayed ratio corresponds to the same individual cell. Scale bar: 10 µm.

(B) Histogram showing plasmolysis ratio (protoplast area to cell area) in root epidermal cells of 5-d-old seedlings expressing YFP-LTI6b in Col-0, *cesa3*^{je5}, or *rhm1-1* background, respectively. Different letters indicate significant differences by one-way ANOVA and Tukey's test. $n \geq 113$ cells from at least 10 seedlings per genotype.

(C) Schematic workflow of the proximity labeling-based mass spectroscopy.

(D) Volcano plot showing differentially enriched proteins in the plasma membrane proteome of *cesa3*^{je5} compared to the wild type Col-0. Significantly enriched or depleted proteins are color coded in blue. Pre-filtering steps removed genetic background from each TbID-YFP-LTI6b-labeled samples using Welch t-test with an FDR of 0.05 and an S0 of 0.5. Pair-wise comparison was then conducted between TbID-YFP-LTI6b/*cesa3*^{je5} and TbID-YFP-LTI6b/Col-0 using Student's *t*-test with an FDR of 0.05 and an S0 of 0.5. $n \geq 3$ biological replicates per genotype.

(E) Volcano plot showing differentially enriched proteins in the plasma membrane proteome of *rhm1-1* compared to the wild type Col-0. Significantly enriched or depleted proteins are color coded in orange. Pre-filtering steps removed genetic background from each TbID-YFP-LTI6b-labeled samples using Welch t-test with an FDR of 0.05 and an S0 of 0.5. Pair-wise comparisons were then conducted between TbID-YFP-LTI6b/*rhm1-1* and TbID-YFP-LTI6b/Col-0 using Student's *t*-test with an FDR of 0.05 and an S0 of 0.5. $n \geq 3$ biological replicates per genotype.

(F) Spinning disk confocal images of GFP-CESA3 in root epidermal cells of 5-d-old seedlings of Col-0, *cesa6*$^{prc1-1}$, and *rhm1-1*. The lower panels show magnified views of the regions outlined by white dashed boxes in the corresponding upper panels. Scale bars: 5 µm (upper panels), 1 µm (lower panels).

(G) Quantification of GFP-CESA3 particle density at the plasma membrane from (F). Error bars indicate SD. Different letters indicate significant differences by one-way ANOVA and Tukey's test. $n \geq 19$ cells from at least 10 seedlings per genotype.

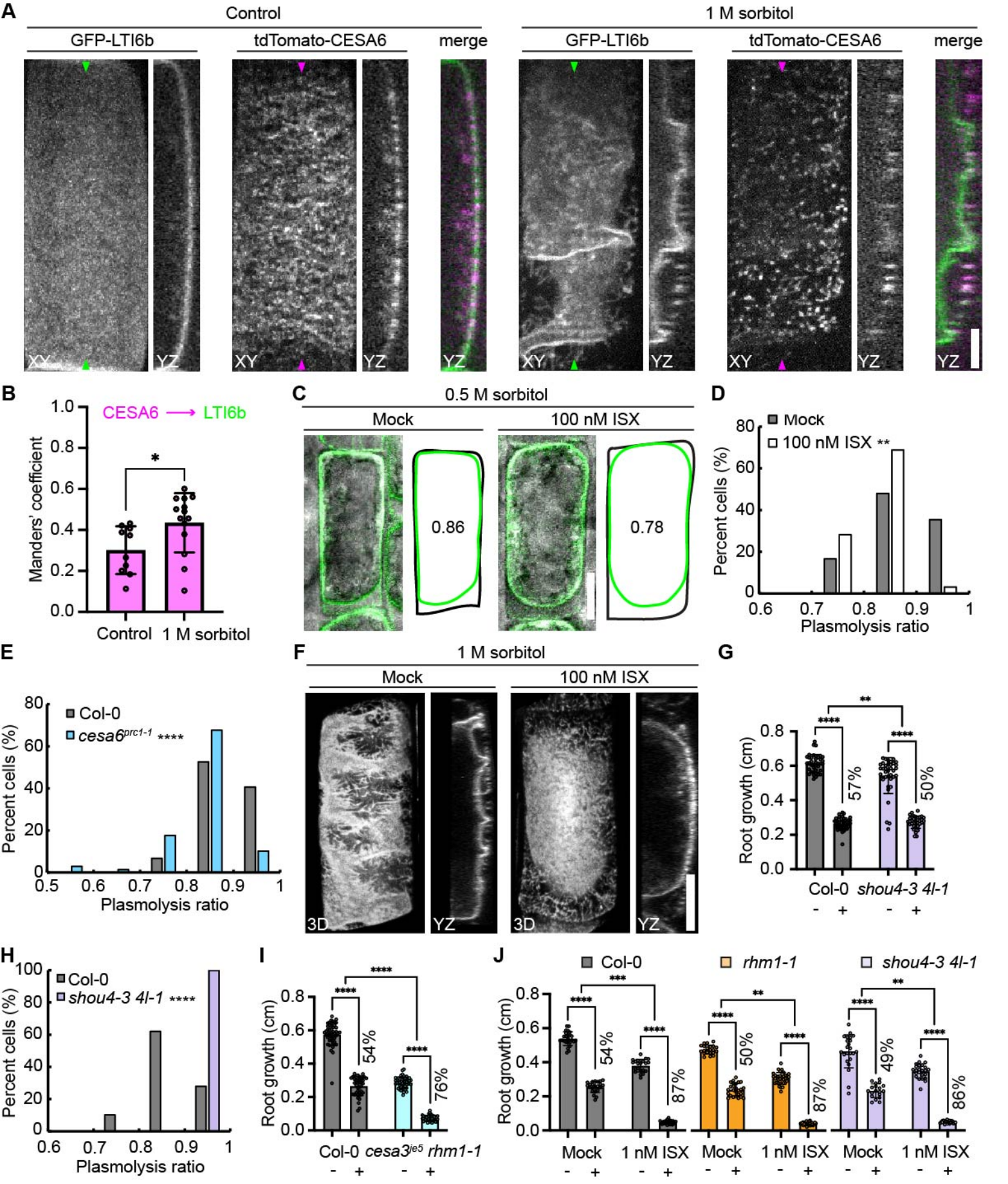
A
Control
1 M sorbitol
GFP-LTI6b
tdTomato-CESA6
merge
XY
YZ
B
CESA6 → LTI6b
Manders' coefficient
Control
1 M sorbitol
C
0.5 M sorbitol
Mock
100 nM ISX
0.86
0.78
D
Mock
100 nM ISX
Percent cells (%)
Plasmolysis ratio
E
Col-0
cesa6prc1-1
Percent cells (%)
Plasmolysis ratio
F
1 M sorbitol
Mock
100 nM ISX
3D
YZ
G
Root growth (cm)
57%
50%
Col-0
shou4-3 4l-1
H
Col-0
shou4-3 4l-1
Percent cells (%)
Plasmolysis ratio
I
Root growth (cm)
54%
76%
Col-0
cesa3je5
rhm1-1
J
Col-0
rhm1-1
shou4-3 4l-1
Root growth (cm)
54%
87%
50%
87%
49%
86%
Mock
1 nM ISX

Figure 4. CSC density at the plasma membrane safeguards wall-membrane attachments and plant growth under hyperosmotic stress.

(A) Spinning disk confocal images of root epidermal cells in 5-d-old seedlings expressing GFP-LTI6b and tdTomato-CESA6 under the control condition or treated with 1 M sorbitol for 5 min. XY and YZ projections are shown. The positions where YZ projections were made are indicated by arrowheads. Scale bar: 5 µm.

(B) Quantification of Manders overlap coeffiicient in 5-d-old seedlings of GFP-LTI6b/tdTomato-CESA6 under the control condition or treated with 1 M sorbitol for 5 min. Error bars indicate SD. $n \geq 10$ cells per genotype per treatment. *$p < 0.05$ by Student's *t*-test.

(C) Laser scanning confocal images and manual tracings of plasmolyzed root epidermal cells in 5-d-old Col-0 seedlings expressing YFP-LTI6b, treated with or without 100 nM isoxaben (ISX) for 20 minutes. Plasmolysis was subsequently induced by treatment with 0.5 M sorbitol for 5 minutes. Each displayed ratio corresponds to the same individual cell. Scale bar: 10 µm.

(D) Histogram showing plasmolysis ratio in root epidermal cells in 5-d-old Col-0 seedlings expressing YFP-LTI6b, treated with or without 100 nM ISX for 20 minutes. $n \geq 32$ cells from at least 5 seedlings per treatment. **$p < 0.01$ by Student's *t*-test.

(E) Histogram showing plasmolysis ratio induced by 0.5 M sorbitol in root epidermal cells of 5-d-old seedlings expressing YFP-LTI6b in Col-0 or *cesa6*$^{prc1-1}$ background, respectively. $n \geq 59$ cells from at least 10 seedlings per genotype. ****$p < 0.0001$ by Student's *t*-test.

(F) 3D renderings and YZ projections of root epidermal cells of 5-d-old YFP-LTI6b seedlings treated with or without 100 nM ISX for 20 minutes. Plasmolysis was subsequently induced by treatment with 1 M sorbitol for 5 minutes. Scale bar: 10 µm.

(G) Root growth of wild type and *shou4-3 4l-1* mutants 1 day after transfer to either fresh MS media (-) or MS media supplemented with 0.28 M sorbitol (+). $n \geq 34$ seedlings per genotype per treatment.

(H) Histogram showing plasmolysis ratio induced by 0.5 M sorbitol in root epidermal cells of 5-d-old seedlings expressing YFP-LTI6b in Col-0 or *shou4-3 4l-1* background, respectively. $n \geq 79$ cells from at least 9 seedlings per genotype. ****$p < 0.0001$ by Student's *t*-test.

(I) Root growth of wild type and *cesa3*^{je5} *rhm1-1* mutants 1 day after transfer to either fresh MS media (-) or MS media supplemented with 0.28 M sorbitol (+). $n \geq 42$ seedlings per genotype per treatment.

(J) Effects of ISX on root growth in wild type, *rhm1-1*, and *shou4-3 4l-1* mutants 1 day after transfer to either fresh MS media (-) or MS media supplemented with 0.28 M sorbitol (+) in the presence or absence of 1 nM ISX. $n \geq 19$ seedlings per genotype per treatment.

Error bars indicate SD. **$p < 0.01$, ***$p < 0.001$, ****$p < 0.0001$ by two-way ANOVA.

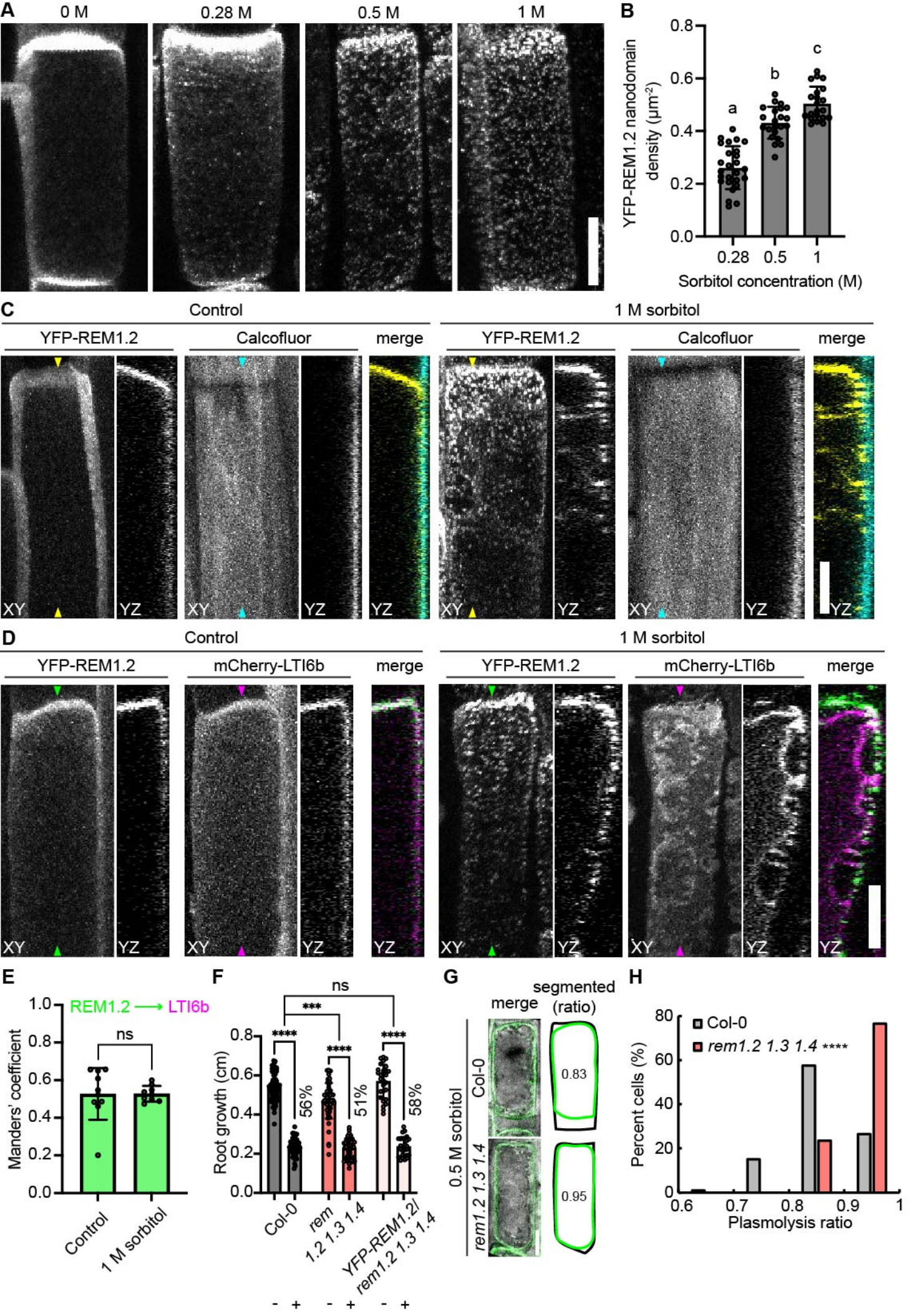
A
0 M
0.28 M
0.5 M
1 M
B
YFP-REM1.2 nanodomain density (µm⁻²)
0.8
0.6
0.4
0.2
0.0
a
b
c
0.28
0.5
1
Sorbitol concentration (M)
C
Control
1 M sorbitol
YFP-REM1.2
Calcofluor
merge
XY
YZ
D
Control
1 M sorbitol
YFP-REM1.2
mCherry-LTI6b
merge
XY
YZ
E
REM1.2 ⟶ LTI6b
Manders' coefficient
1.0
0.8
0.6
0.4
0.2
0.0
ns
Control
1 M sorbitol
F
Root growth (cm)
0.8
0.6
0.4
0.2
0.0
ns
***
****
56%
51%
58%
Col-0
rem 1.2 1.3 1.4
YFP-REM1.2/ rem1.2 1.3 1.4
- + - + - +
G
merge
segmented (ratio)
0.5 M sorbitol
Col-0
rem1.2 1.3 1.4
0.83
0.95
H
Percent cells (%)
80
60
40
20
0
Col-0
rem1.2 1.3 1.4 ****
0.6
0.7
0.8
0.9
1
Plasmolysis ratio

Figure 5. The rapidly forming REM nanodomains function as negative regulators of wall-membrane attachments

(A) Laser scanning confocal images in root epidermal cells of 5-d-old seedlings expressing YFP-REM1.2 treated with 0 M, 0.28 M, 0.5 M, or 1 M sorbitol for 5 min, respectively. Scale bar: 10 μm.

(B) Bar graph showing YFP-REM1.2 nanodomain density at different sorbitol concentrations quantified from (A). $n \geq 21$ cells from at least 5 seedlings per treatment. Error bars indicate SD. Different letters indicate significant differences by one-way ANOVA and Tukey's test.

(C) Laser scanning confocal images of root epidermal cells in 5-d-old seedlings expressing YFP-REM1.2 co-stained with calcofluor white under the control condition or treated with 1 M sorbitol for 5 min. XY and YZ projections are shown. The positions where YZ projections were made are indicated by arrowheads. Scale bar: 10 μm.

(D) Laser scanning confocal images of root epidermal cells in 5-d-old seedlings expressing YFP-REM1.2 and mCherry-LTI6b under the control condition or treated with 1 M sorbitol for 5 min. XY and YZ projections are shown. The positions where YZ projections were made are indicated by arrowheads. Scale bar: 10 μm.

(E) Quantification of Manders overlap coeffiicient in 5-d-old seedlings of YFP-REM1.2/mCherry-LTI6b under the control condition or treated with 1 M sorbitol for 5 min. Error bars indicate SD. $n \geq 9$ cells per genotype per treatment. ns, no significance by Student's *t*-test.

(F) Root growth of wild type, *rem1.2 1.3 1.4* triple mutants, and *YFP-REM1.2*/*rem1.2 1.3 1.4* lines 1 day after transfer to either fresh MS media (-) or MS media supplemented with 0.28 M sorbitol (+). $n \geq 27$ seedlings per genotype per treatment. Error bars indicate SD. ns, no significance; ***$p < 0.001$, ****$p < 0.0001$ by two-way ANOVA.

(G) Laser scanning confocal images and manual tracings of plasmolyzed root epidermal cells in 5-d-old seedlings expressing YFP-LTI6b in Col-0 or *rem1.2 1.3 1.4* background, respectively. Plasmolysis was induced by 0.5 M sorbitol for 5 min. Each displayed ratio corresponds to the same individual cell. Scale bar: 10 μm.

(H) Histogram showing plasmolysis ratio in root epidermal cells of 5-d-old seedlings expressing YFP-LTI6b in Col-0 or *rem1.2 1.3 1.4* background, respectively. $n \geq 102$ cells from at least 10 seedlings per genotype. ****$p < 0.0001$ by Student's *t*-test.

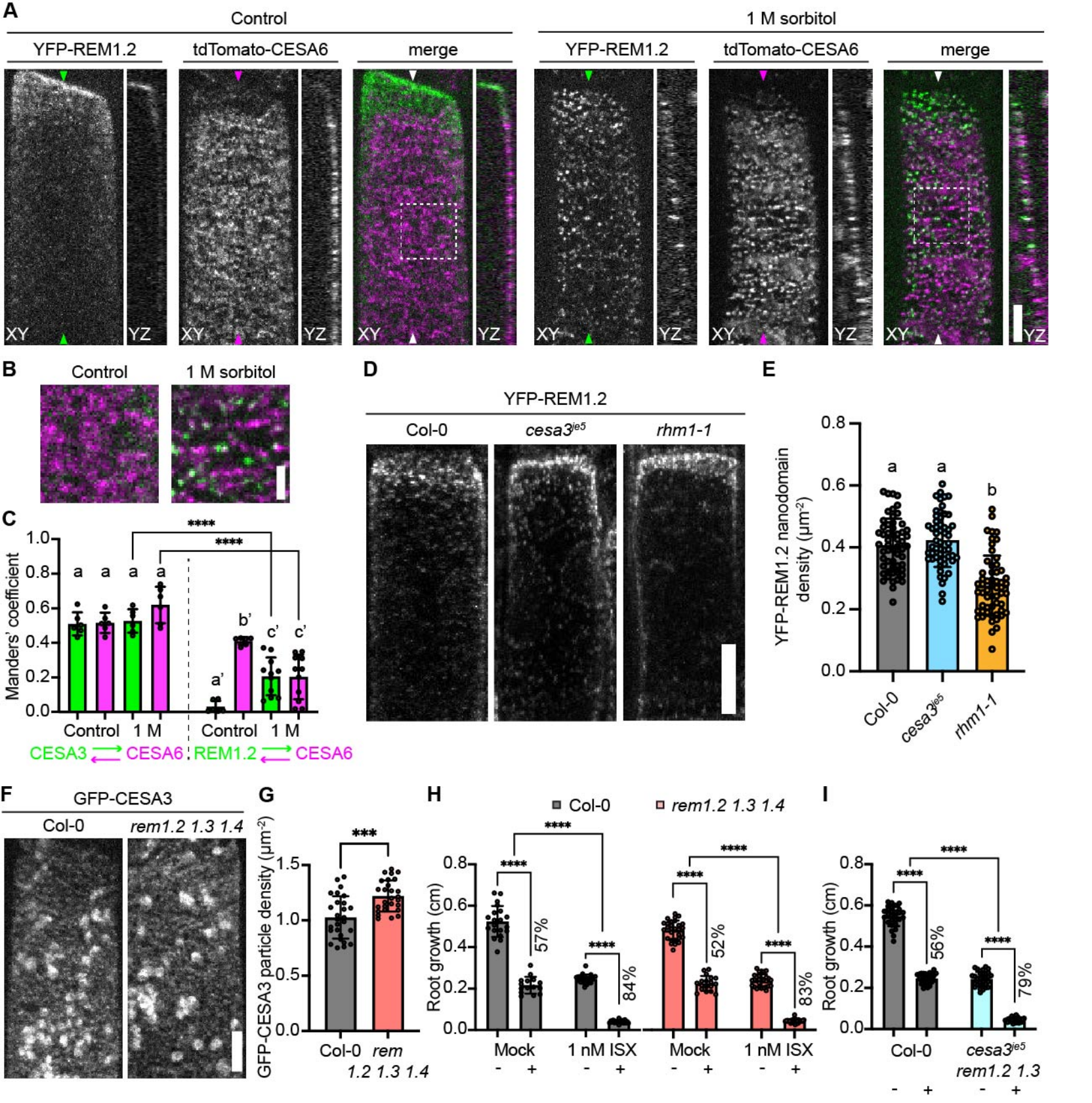
A
Control
1 M sorbitol
YFP-REM1.2
tdTomato-CESA6
merge
XY
YZ
B
Control
1 M sorbitol
C
Manders' coefficient
Control
1 M
CESA3
CESA6
REM1.2
D
YFP-REM1.2
Col-0
cesa3je5
rhm1-1
E
YFP-REM1.2 nanodomain density (μm-2)
F
GFP-CESA3
rem1.2 1.3 1.4
G
GFP-CESA3 particle density (μm-2)
H
Col-0
rem1.2 1.3 1.4
Root growth (cm)
Mock
1 nM ISX
57%
84%
52%
83%
I
56%
79%

Figure 6. REMs antagonize CSCs to regulate hyperosmotic stress responses.

(A) Spinning disk confocal images of root epidermal cells in 5-d-old seedlings expressing YFP-REM1.2 and tdTomato-CESA6 under the control condition or treated with 1 M sorbitol for 5 min. XY and YZ projections are shown. The positions where YZ projections were made are indicated by arrowheads. Scale bar: 5 μm.

(B) Magnified views of the regions outlined by white dashed boxes in (A). Scale bar: 2 μm.

(C) Quantification of Manders overlap coeffiicient in 5-d-old seedlings of GFP-CESA3/tdTomato-CESA6 or YFP-REM1.2/tdTomato-CESA6 under the control condition or treated with 1 M sorbitol for 5 min. Error bars indicate SD. $n \geq 6$ cells per genotype per treatment. In each genotype, different letters indicate significant differences by one-way ANOVA and Tukey's test. ****$p < 0.0001$ by Student's *t*-test when comparing the two genotypes under the same condition.

(D) Laser scanning confocal images of YFP-REM1.2 nanodomains in 5-d-old seedlings of the Col, *cesa3*^{je5}, or *rhm1-1* background, respectively when treated with 0.5 M sorbitol for 5 min. Scale bar: 10 μm.

(E) Quantification of YFP-REM1.2 nanodomain density from (C). $n \geq 54$ cells from at least 10 seedlings per genotype. Error bars indicate SD. Different letters indicate significant differences by one-way ANOVA and Tukey's test.

(F) Spinning disk confocal images of GFP-CESA3 in root epidermal cells of 5-d-old seedlings of Col and *rem1.2 1.3 1.4.* Scale bar: 5 μm.

(G) Quantification of GFP-CESA3 particle density at the plasma membrane from (E). $n = 27$ cells from at least 6 seedlings per genotype. Error bars indicate SD. ***$p < 0.001$ by Student's *t*-test.

(H) Effects of ISX on root growth in wild type and *rem1.2 1.3 1.4* mutants 1 day after transfer to either fresh MS media (-) or MS media supplemented with 0.28 M sorbitol (+) in the presence or absence of 1 nM ISX. $n \geq 15$ seedlings per genotype per treatment.

(I) Root growth of wild type and *cesa3*^{je5} *rem1.2 1.3* mutants 1 day after transfer to either fresh MS media (-) or MS media supplemented with 0.28 M sorbitol (+). $n \geq 28$ seedlings per genotype per treatment.
Error bars indicate SD. ****$p < 0.0001$ by two-way ANOVA.

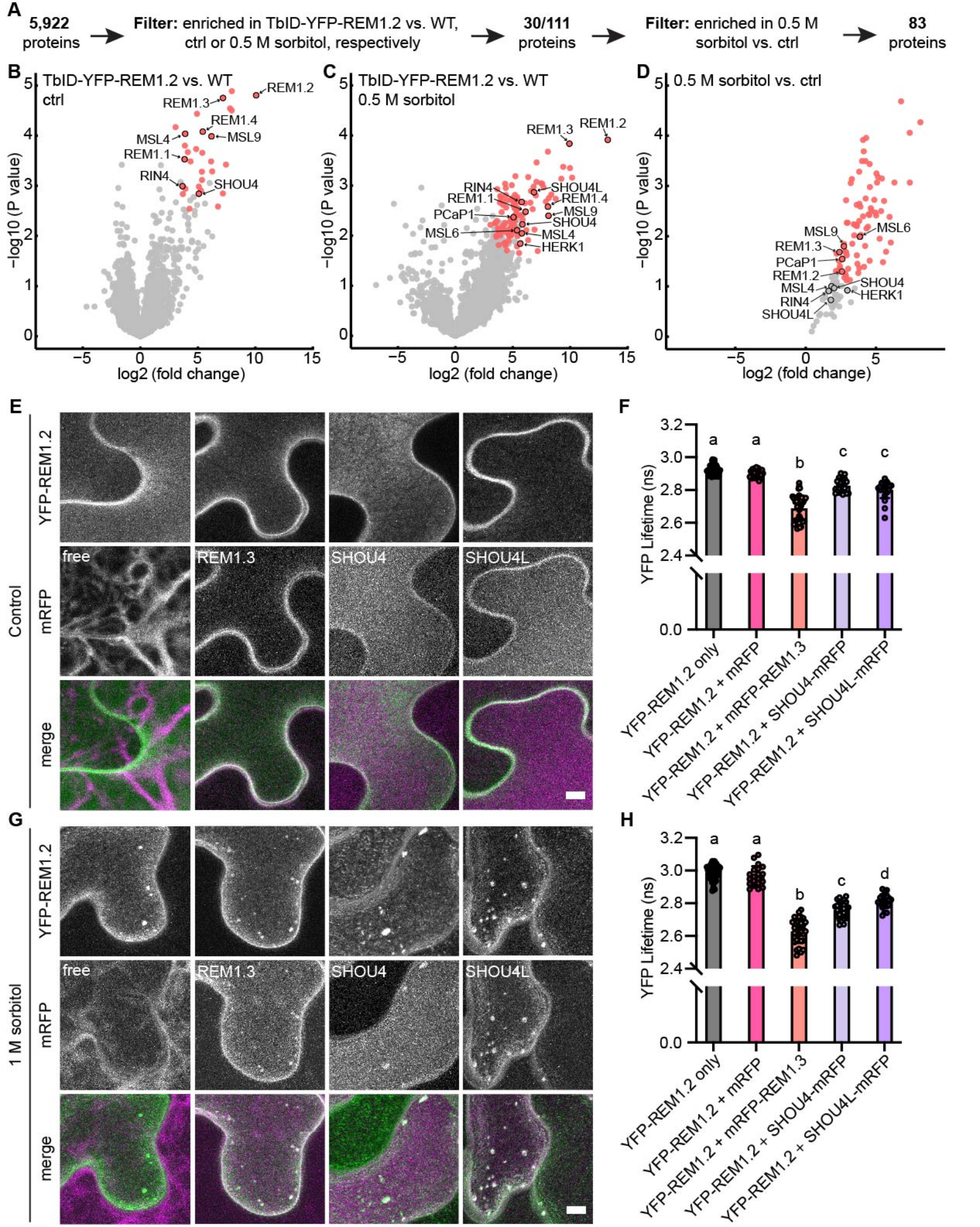
A
5,922 proteins
Filter: enriched in TbID-YFP-REM1.2 vs. WT, ctrl or 0.5 M sorbitol, respectively
30/111 proteins
Filter: enriched in 0.5 M sorbitol vs. ctrl
83 proteins
B
TbID-YFP-REM1.2 vs. WT
ctrl
REM1.2
REM1.3
REM1.4
MSL4
MSL9
REM1.1
RIN4
SHOU4
−log10 (P value)
log2 (fold change)
C
TbID-YFP-REM1.2 vs. WT
0.5 M sorbitol
REM1.3
REM1.2
RIN4
SHOU4L
REM1.1
REM1.4
PCaP1
MSL9
SHOU4
MSL6
MSL4
HERK1
D
0.5 M sorbitol vs. ctrl
MSL9
MSL6
REM1.3
PCaP1
REM1.2
SHOU4
MSL4
HERK1
RIN4
SHOU4L
E
Control
YFP-REM1.2
mRFP
merge
free
REM1.3
SHOU4
SHOU4L
F
YFP Lifetime (ns)
YFP-REM1.2 only
YFP-REM1.2 + mRFP
YFP-REM1.2 + mRFP-REM1.3
YFP-REM1.2 + SHOU4-mRFP
YFP-REM1.2 + SHOU4L-mRFP
G
1 M sorbitol
YFP-REM1.2
mRFP
merge
free
REM1.3
SHOU4
SHOU4L
H
YFP Lifetime (ns)
YFP-REM1.2 only
YFP-REM1.2 + mRFP
YFP-REM1.2 + mRFP-REM1.3
YFP-REM1.2 + SHOU4-mRFP
YFP-REM1.2 + SHOU4L-mRFP

Figure 7. REM nanodomains harbor many other proteins in the vicinity, including SHOU4/4L.

(A) Workflow of filtering steps to identify proteins in the vicinity of TbID-YFP-REM1.2 in the presence or absence of 0.5 M sorbitol.

(B) and (C) Volcano plots showing differentially enriched proteins comparing TbID-YFP-REM1.2/Col-0 and Col-0 (WT) under the control (ctrl) condition (B) or treated with 0.5 M sorbitol for 15 min (C). Significantly enriched proteins are color coded using one-sided Welch's *t*-test with an FDR of 0.05 and an S0 of 0.5. $n \geq 3$ biological replicates.

(D) Volcano plot showing differentially enriched proteins comparing 0.5 M sorbitol treatment and the control condition in TbID-YFP-REM1.2/Col-0. Pair-wise comparison was conducted using Student's *t*-test with an FDR of 0.05 and an S0 of 0.5. $n \geq 3$ biological replicates.

(E) Laser scanning confocal images of tobacco leaf epidermal cells co-expressing YFP-REM1.2 with free mRFP, mRFP-REM1.3, SHOU4-mRFP, or SHOU4L-mRFP, respectively, under control conditions. Scale bar: 5 µm.

(F) Measurements of YFP lifetime from (E). Error bars indicate SD. Different letters indicate significant differences by one-way ANOVA and Tukey's test. $n \geq 23$ regions of interest from at least 3 infiltrated plants per construct combination.

(G) Laser scanning confocal images of tobacco leaf epidermal cells co-expressing YFP-REM1.2 with free mRFP, mRFP-REM1.3, SHOU4-mRFP, or SHOU4L-mRFP, respectively, upon 1 M sorbitol treatment for 10 min. Scale bar: 5 µm.

(H) Measurements of YFP lifetime from (E). Error bars indicate SD. Different letters indicate significant differences by one-way ANOVA and Tukey's test. $n \geq 20$ regions of interest from at least 3 infiltrated plants per construct combination.